JGR Solid Earth

RESEARCH ARTICLE
10.1029/2019JB018508

Geochemical Evidence for Hydration and Dehydration of Crustal Rocks During Continental Rifting

Qiang He[1,2], Shao-Bing Zhang[1,2], Yong-Fei Zheng[1,2], Qiong-Xia Xia[1,2], and Daniela Rubatto[3,4]

[1]CAS Key Laboratory of Crust-Mantle Materials and Environments, School of Earth and Space Sciences, University of Science and Technology of China, Hefei, China, [2]Center of Excellence for Comparative Planetology, Chinese Academy of Sciences, Hefei, China, [3]Research School of Earth Sciences, Australian National University, Canberra, ACT, Australia, [4]Institute of Geological Sciences, University of Bern, Bern, Switzerland

Abstract To understand the temporal sequence of geological processes such as magmatism, water-rock interaction, and metamorphism in fossil continental rifts, a combined study of petrography, mineral geochemistry, in situ garnet O isotopes, in situ zircon U-Pb ages and O isotopes, and pseudosection calculations was conducted for metagranites from a Neoproterozoic continental rift generated during the Rodinia breakup. The results provide insights into the operation of hydration and dehydration during continental rifting. In the metagranites from the northern margin of South China, three types of garnet (Garnet-I to -III) are distinguished. They were sequentially produced by hydrothermal alteration, metamorphic dehydration, and fluid metasomatism. All of these garnets show negative $\delta^{18}O$ values of −19.3‰ to −14.5‰, in contrast to mantle-like $\delta^{18}O$ values for magmatic zircon. The extremely negative $\delta^{18}O$ values of hydrothermal Garnet-I require infiltration of the continental deglacial meltwater during the continental rifting, and before that zircon crystallized from normal $\delta^{18}O$ magmas. Once the rocks were hydrothermally altered, the extreme ^{18}O depletion was retained in all later products such as metamorphic Garnet-II and metasomatic Garnet-III. Pseudosection calculations indicate that the metamorphic dehydration occurred at 1.0–3.0 kbar and 630–690 °C during a reheating stage, corresponding to high thermal gradients of >60 °C/km. The high-temperature/low-pressure metamorphic rocks produced by such high thermal gradients are indicative of the continental rift setting. The mineral geochemistry records not only the temporal sequence of rift magmatism, water-rock interaction, and rift metamorphism but also the evolution of temperature and water action in the crust during the continental rifting.

Key Points:
- Garnets record sequential operation of hydrothermal alteration, metamorphic dehydration, and albitization during the continental rifting
- Penetration of the surface water occurred at a time between the magmatic zircon growth and subsequent rift metamorphism
- Metamorphic rocks that record high thermal gradients are indicative of continental rifting

Supporting Information:
- Supporting Information S1

Correspondence to:
Q. He and S.-B. Zhang,
heq7224@mail.ustc.edu.cn;
sbzhang@ustc.edu.cn

Citation:
He, Q., Zhang, S.-B., Zheng, Y.-F., Xia, Q.-X., & Rubatto, D. (2019). Geochemical evidence for hydration and dehydration of crustal rocks during continental rifting. *Journal of Geophysical Research: Solid Earth*, *124*. https://doi.org/10.1029/2019JB018508

Received 7 AUG 2019
Accepted 14 NOV 2019
Accepted article online 5 DEC 2019

1. Introduction

Continental rifts are tectonic zones where lithosphere extension results in its possible rupture and eventually creation of new ocean basins (Dewey & Burke, 1974; Olsen, 1995; Ruppel, 1995; Wilson, 1966). The extension during continental rifting leads to not only transient thermal pulses but also permanent structural and compositional modification of the rifting lithosphere (Olsen, 1995; Zheng & Chen, 2017). In general, this leads to asthenospheric upwelling for rift magmatism and crustal subsidence for basin sedimentation (McKenzie, 1978; White et al., 1987). Its products are rift basin sedimentary rocks (Cloetingh & Wortel, 1986; Sengör & Burke, 1978; Wang & Li, 2003) and bimodal volcanics (Giese & Bühn, 1994; Li et al., 2002; Li, Li, et al., 2008). Furthermore, it also results in Buchan-type amphibolite to granulite facies metamorphic rocks at converged plate boundaries (He et al., 2018; Hermann & Rubatto, 2003; Zheng et al., 2019; Zheng & Chen, 2017). The metamorphic rocks of Buchan facies series are vital to recognizing fossil continental rifts and reconstructing the tectonic evolution of ancient blocks (Zheng & Zhao, 2017). However, these lithotectonic records are frequently obliterated by superimposition of later geological processes (Buck, 2015; Zheng & Chen, 2017; Ziegler & Cloetingh, 2004), resulting in difficulties in the identification of fossil continental rifts. Nevertheless, the tectonic evolution of a continental rift can be reconstructed by using refractory minerals that preserve the record of transient thermal pulses despite later modifications. In addition, surface water-rock interaction was once active in fossil continental rifts, leaving us a sensitive indicator in refractory minerals, that is, low to negative $\delta^{18}O$ values, to trace fluid action in fossil continental rifts (Bindeman et al., 2010; Bindeman & Serebryakov, 2011; He et al., 2016; Zheng et al., 2007).

An important issue is how refractory minerals acquire their low to negative $\delta^{18}O$ values in geological processes. Rock-forming minerals in low to negative $\delta^{18}O$ rocks can be categorized into two groups in terms of their response to fluid action (King et al., 1997; O'Neil & Taylor, 1967; Zheng & Fu, 1998). One is fluid-susceptible (e.g., feldspars and micas), and the other is fluid-resistant (usually refractory, e.g., garnet and zircon). Fluid-susceptible minerals (including hydrothermally grown ones) can acquire low to negative $\delta^{18}O$ signatures directly from the surface water by hydrothermal alteration. For fluid-resistant minerals to obtain the ^{18}O depleted signature, it is necessary to have two-stage processes of hydrothermal alteration and reheating (Zheng et al., 2004, 2007). On the other hand, high-temperature (HT) metamorphism at low pressure (LP) is favored during continental rifting (Bertotti et al., 1993; He et al., 2018; Hermann & Rubatto, 2003; Trommsdorff et al., 1993; Wickham & Oxburgh, 1985, 1986; Zheng & Chen, 2017). At elevated temperatures, crustal rocks may undergo partial melting during continental rifting (Zheng & Chen, 2017). In this case, low to negative $\delta^{18}O$ signatures can be transferred from hydrothermally altered, fluid-susceptible minerals into later metamorphic and magmatic products, including some fluid-resistant minerals (Bindeman et al., 2010; Bindeman & Serebryakov, 2011; Bindeman & Valley, 2000; He et al., 2016, 2018; Tang et al., 2008; Zheng et al., 2004, 2007). As a consequence, the O isotopic and chemical compositions of refractory minerals can faithfully record the complex processes in continental rifts, providing an alternative approach to identify fossil continental rifts.

Previous studies have revealed that relict zircon in ultrahigh-pressure (UHP) metamorphic rocks can survive during subduction zone metamorphism and preserve the primary negative $\delta^{18}O$ signature of igneous protolith acquired by continental rift magmatism due to meteoric hydrothermal alteration at high temperature (He et al., 2016; Tang et al., 2008). In this study, we focus on garnet, another refractory mineral, to investigate the hydration and dehydration of crustal rocks in a fossil continental rift. Garnet can be produced by both hydrothermal alteration (Jamtveit et al., 1993) and metamorphic dehydration (Baxter & Caddick, 2013; Dragovic et al., 2015; Le Breton & Thompson, 1988; Spear & Kohn, 1996). Thus, it has a potential to record the complex processes in continental rifts and unravel the temporal sequence of their operation. Garnet can grow in a wide range of rock compositions and pressure-temperature (P-T) conditions (Baxter et al., 2013). It has a strong capacity to preserve its chemical and isotopic compositions (Vielzeuf et al., 2005). Therefore, garnet geochemistry has been used to estimate the P-T conditions (e.g., Holdaway, 2000) and constrain its formation mechanism (Hermann & Rubatto, 2003; Hickmott et al., 1987; Lackey et al., 2011; Spear & Kohn, 1996). In terms of fluid infiltration and flow behavior, garnet O isotope composition is a sensitive indicator to water-rock interaction (Chamberlain & Conrad, 1991; Crowe et al., 2001; D'Errico et al., 2012; Russell et al., 2013). In combination with zircon O isotopes and U-Pb ages, garnet can be used to reconstruct multiple episodes of fluid action in metamorphic rocks (e.g., Martin et al., 2014; Page et al., 2014; Rubatto & Angiboust, 2015). In addition, garnet can be directly dated by Sm-Nd and Lu-Hf radiometric methods (Baxter et al., 2017; Baxter & Scherer, 2013).

Garnet in metagranites from the Beihuaiyang zone in the northern margin of the Dabie orogen satisfies all of the requirements for investigating fluid-rock interaction during continental rifting. First, there is widespread ^{18}O depletion in the Dabie-Sulu orogenic belt (Zheng et al., 2003, 2009), which has been ascribed to meteoric-hydrothermal alteration in a continental rift setting in the Middle Neoproterozoic (Zheng et al., 2004, 2007, 2008). Second, meteoric-hydrothermal alteration and low $\delta^{18}O$ magmatism have been reported in the Beihuaiyang zone (Wu et al., 2007; Zheng et al., 2007). Third, garnet in the metagranites from the Beihuaiyang zone was analyzed for the bulk O isotope composition by the laser fluorination technique, yielding negative $\delta^{18}O$ value as low as −14.4‰ (Zheng et al., 2007). Petrographic observations of garnet morphology and zoning reveal different garnet types, which may be related to different stages of continental rifting. However, the laser analysis gave a weighted mean of $\delta^{18}O$ values for multiple garnet grains, failing to distinguish between the $\delta^{18}O$ values of different garnet types. In addition, the bulk O isotope analysis could be influenced by the presence of mineral inclusions. In order to distinguish between the different origins of garnet, a microscale secondary ion mass spectroscopy (SIMS) garnet O isotope analysis was performed in this study. In combination with petrography, mineral geochemistry, in situ zircon U-Pb ages and O isotopes, the results provide insights into the operation of hydration and dehydration during the continental rifting. This enables identification of the fossil continental rift at the converged continental boundary.

2. Geological Setting and Samples

The Beihuaiyang zone is located in the northern margin of the Dabie orogen (Figure 1). The Dabie orogen, together with the Sulu orogen in east central China, were generated by northward subduction of the South China Block beneath the North China Block in the Triassic (Ernst et al., 2007; Zheng et al., 2009). On the one hand, the continental crust was subducted to subarc depths for Alpine-type metamorphism, producing abundant eclogite-facies high-pressure (HP) to ultrahigh-pressure (UHP) metamorphic rocks in the Dabie-Sulu orogenic belt (Liou et al., 2012; Zheng et al., 2003, 2019). On the other hand, part of crustal rocks was only subducted to shallow depths, giving rise to low-grade metamorphic rocks at greenschist facies with variable degrees of deformation in the Beihuaiyang zone (Hacker et al., 1998; Zheng et al., 2005). Nevertheless, both high- and low-grade metamorphic rocks share the same composition of protoliths that are dominated by mafic and felsic magmatic rocks of Middle Neoproterozoic age (Chen et al., 2003; Hacker et al., 1998; He et al., 2018; Wu et al., 2007; Zheng et al., 2004; Zheng et al., 2006; Zheng et al., 2007).

The Beihuaiyang zone is composed of Upper Neoproterozoic to Lower Paleozoic flysch sediments (the Foziling Group) and Neoproterozoic intrusives (the Luzhenguan complex). These magmatic intrusives have been regarded as the product of continental rift magmatism during the Rodinia breakup (He et al., 2018; Wu et al., 2007; Zheng et al., 2004, 2005, 2007, 2008). Zircon U-Pb dating of these intrusives yields concordant ages of 740–780 Ma, consistent with the known age for the Rodina breakup in the Middle Neoproterozoic (Li et al., 2003, Li, Bogdanova, et al., 2008). In terms of a combined structural, petrological and geochronological study, Zheng et al. (2005) conclude that the Beihuaiyang zone represents an accretionary wedge that was offscrapped from the subducting continental lithosphere of the South China Block at shallow depths of <10 km. In this regard, this zone is the weakest metamorphosed part relative to those HP to UHP metamorphic zones in the Dabie orogen. This weakly metamorphosed zone has preserved the primary mineral texture and composition of its protoliths that formed during granite emplacement and subsequent subsolidus processes in the Middle Neoproterozoic (He et al., 2018; Zheng et al., 2007).

In the Middle Neoproterozoic, a series of continental rifts were developed along the Grenvillian orogens in supercontinent Rodinia in response to its failed and successful rifting for breakup. While many of these rifts did not run into lithospheric rupture, one along the northern margin of the South China Block (the present coordinate) was successful to result in its separation from the other continental blocks such as Australia and India (Li et al., 2003, Li, Bogdanova, et al., 2008; Zhang & Zheng, 2013; Zheng et al., 2013). This continental rifting is similar to the opening of Atlantic Ocean along a former collisional orogen (Dewey & Burke, 1974; Wilson, 1966). Evidence for the continental rifting system during the Rodinia breakup is partially preserved in the northern margin of the South China Block, including bimodal volcanics and low $\delta^{18}O$ magmatic rocks (Fu et al., 2013; He et al., 2016; Tang et al., 2008; Wang et al., 2010; Wang & Li, 2003; Zheng et al., 2004, 2007). Pseudosection calculations for metagranites from the Beihuaiyang zone yield 1.0–3.5 kbar and 560–660 °C for the HT/LP metamorphism (He et al., 2018), indicating high thermal gradients during the continental rifting. Therefore, the rocks in this area experienced the Buchan-type amphibolite-facies metamorphism during the continental rifting in the Middle Neoproterozoic. Nevertheless, these rocks were overprinted by the greenschist-facies metamorphism during the continental collision in the Triassic.

Samples used in the present study are garnet-bearing gneissic metagranites from Wozicun in the Beihuaiyang zone. Metagranites 07BHY01, 14BHY02, and 14BHY08 were collected from a road cut about 20 m long and metagranites 14BHY18, 14BHY27, and 14BHY35 from another profile about 1 km east. The metagranites are generally light gray and coarse grained. They are composed of quartz, plagioclase and K-feldspar, garnet, and variable proportions of biotite and muscovite. Accessory zircon and minor epidote and zoisite are also observed.

3. Analytical Methods

After rock samples were crushed and sieved, mineral grains (zircon and garnet) were separated by heavy liquid and magnet techniques, handpicked under a binocular microscope, and then mounted in epoxy resin. They were polished to expose their interior. Cathodoluminescence (CL) and back-scattered electron (BSE) imaging were used to determine the internal zoning of zircon and garnet crystals, respectively. Thin sections were observed carefully under an optical microscope. For a representative thin section of metagranite

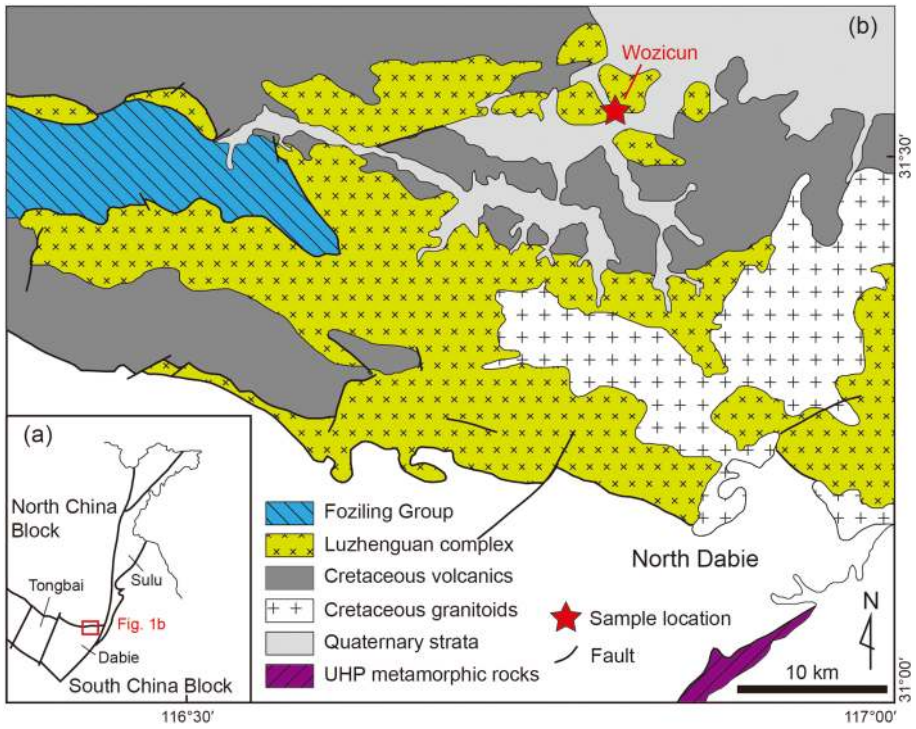

Figure 1. (a) Position of the Beihuaiyang zone in the northern margin of the South China Block. (b) A simplified geological map for the Beihuaiyang zone in the Dabie-Sulu orogenic belt. The red star indicates the sampling location.

14BHY08, major element distribution was scanned using a Bruker M4 Tornado micro-X-ray fluorescence (μXRF) instrument and mineral proportions were calculated accordingly.

SIMS zircon U-Pb dating and O isotope analysis were conducted using a CAMECA IMS-1280 ion microprobe at State Key Laboratory of Lithospheric Evolution in Institute of Geology and Geophysics, Chinese Academy of Sciences, Beijing. For the U-Pb dating, analytical procedures, Pb/U calibration and calculation of U and Th contents were the same as those described by Li et al. (2009). Correction to the common lead was made using the measured ^{204}Pb and the model crustal Pb isotope compositions (Stacey & Kramers, 1975). Zircon U-Pb data were handled using Isoplot/Ex_ver3.23 (Ludwig, 2003). For the O isotope analysis, the instrumentation and operating conditions were described in detail by Li, Li, et al. (2010). The instrumental mass fractionation was corrected using an internal zircon standard Penglai with $\delta^{18}O_{VSMOW} = 5.31 \pm 0.10‰$ (Li, Long, et al., 2010). Zircon 91500 was used as a secondary in-house standard to monitor the data quality. During the two analysis sessions, the δ^{18}O values for 91500 are 10.28 ± 0.38‰ (n = 7, Mean standard weighted deviation (MSWD) = 3.4) and 10.21 ± 0.20‰ (n = 4, MSWD = 2.4). Correction to the instrumental mass fractionation was done following the details described by Li, Li, et al. (2010). The corrected δ^{18}O values are reported in the standard per mil notation, along with 2 standard error.

Major element compositions of garnet, biotite, and plagioclase were measured using a Shimazu EPMA 1600 electron microprobe at Chinese Academy of Sciences Key Laboratory of Crust-Mantle Materials and Environments in University of Science and Technology of China, Hefei. The accelerating voltage was set as 15 kV. The beam current was variable for different minerals, that is, 10 nA for biotite, 15 nA for plagioclase, and 20 nA for garnet. Natural silicate standards were used, and raw data were reduced using conventional atomic number, absorption, fluorescence (ZAF) correction procedures. Beam size was normally set as 1 μm except that a defocused beam of 10 μm was used for feldspars to minimize the loss of Na and K during the analyses.

Garnet trace element analysis by laser ablation-inductively coupled plasma mass spectrometry was conducted at State Key Laboratory of Geological Processes and Mineral Resources in China University of Geosciences, Wuhan. Laser sampling was performed using an excimer laser ablation system (GeoLas

2005). An Agilent 7500a ICP-MS instrument was used to acquire ion signal intensities. Analytical procedures followed those described by Liu et al. (2008). Analysis spot size was 32 μm. Off-line selection, integration of background and analytical signals, time drift correction, and quantitative calibration was conducted using ICPMSDataCal (Liu et al., 2010). Trace element concentrations were calibrated using multiple reference materials NIST610, BCR-2G, BHVO-2G, and BIR-1G as external standards.

In situ garnet O isotopes were measured on sensitive high resolution ion microprobe – stable isotope (SHRIMP–SI) at the Research School of Earth Sciences, Australian National University (ANU), following the method of Martin et al. (2014). Each analysis consists of six scans of 20 s for a total counting time of 120 s. Garnet compositions were analyzed at the same spot as O isotope analysis by energy dispersive spectroscopy (EDS) using a JEOL JSM-6400 at the Centre for Advanced Microscopy, ANU. The main matrix effects during SHRIMP analysis of O isotopes are related to variation in CaO, MnO, and Fe_2O_3 (Martin et al., 2014). None of the garnet analyses shows any significant andradite component. Therefore, the matrix effect was corrected based on variations in the grossular (Grs) and spessartine (Sps) components. The bias caused by grossular and spessartine components was corrected following these equations: bias (Grs) = $-9.44X^2$(Grs) + 11.86X(Grs) − 1.34, and bias (Sps) = $-5.46X^2$(Sps) + 7.30X(Sps) − 0.12.

The matrix correction curves were acquired by analyzing a set of garnet reference materials covering grossular, andradite, and spessartine, over a large compositional range covering that of the investigated samples (Martin et al., 2014). The 13 reference garnets were checked in the ANU laboratory over several years, and variations in the matrix correction curve over time are within ±0.5‰. Even matrix corrections acquired in different laboratories vary only slightly in the garnet compositional range of interest (Ickert & Stern, 2013; Martin et al., 2014; Page et al., 2010). Garnet standard UWG-2 ($\delta^{18}O = 5.8‰$, Valley et al., 1995) was measured every four unknowns to correct for instrumental mass fractionation and monitor repeatability during the analytical session, and the 10 analyses gave a weighted mean value of 5.81 ± 0.23‰ (1 standard deviation). There are general agreements between the SIMS and laser oxygen isotope data (see below), lending further support to the accuracy of SIMS values. Error propagation for the SIMS O isotope analysis follows Martin et al. (2014).

Phase relations for stable mineral assemblages in metagranite 14BHY08 were constructed in the MnNCKFMASH system using THERMOCALC v. 3.33 (Powell & Holland, 1988) with the internally consistent thermodynamic data set ds55 (Holland & Powell, 1998, updated in October 2009). The bulk composition of metagranite 14BHY08 has been reported by He et al. (2018). Activity-composition relations for solid-solution phases are as follows: garnet and biotite (White et al., 2005); cordierite (Holland & Powell, 1998); orthopyroxene (Powell & Holland, 1999); plagioclase-K-feldspar (Holland & Powell, 2003); and muscovite-paragonite (Coggon & Holland, 2002). Pure phases include sillimanite, andalusite, quartz, and H_2O. The incorporation of Mn into biotite and cordierite follows Mahar et al. (1997). The melt was modeled in the NCKFMASH system on an 8-oxygen basis following White et al. (2007).

4. Results

4.1. Petrography

Fine-grained metagranite 14BHY27 contains a coarse-grained felsic vein which is mainly composed of quartz, K-feldspar and plagioclase with grain size generally greater than 2 mm (Figure 2a). A garnet grain about 100 μm is observed in the vein (Figure 2b). In metagranite 14BHY08, most garnet grains are intimately intergrown with biotite (Figures 2c and 2e). They are anhedral to subhedral with sizes of 200–400 μm. The intergrown biotite is subhedral to anhedral with inward penetrating shapes by garnet grains, suggesting the breakdown of biotite during the growth of garnet (Figure 2c). In some cases, the biotite has been totally consumed (Figure 2d). In one instance, garnet shows a corona around anhedral biotite (Figure 2e), indicating garnet was generated through biotite consumption. Garnet grains in metagranites 14BHY02, 14BHY18, and 14BHY35 are subhedral to euhedral with sizes of 100–200 μm and coexist with muscovite and plagioclase or K-feldspar (Figures 2f–2i). The garnet and muscovite grains are enclosed in plagioclase (Figure 2g) or distributed in the matrix and weakly aligned along the margin of plagioclase or K-feldspar (Figures 2h and 2i). The plagioclase and K-feldspar grains commonly occur as large crystals with grain sizes of 0.5–2.5 mm. The plagioclase contains substantial microscopic pores filled with numerous fine-grained muscovite inclusions. Plagioclase in metagranite 14BHY18 shows more pores than that in metagranite

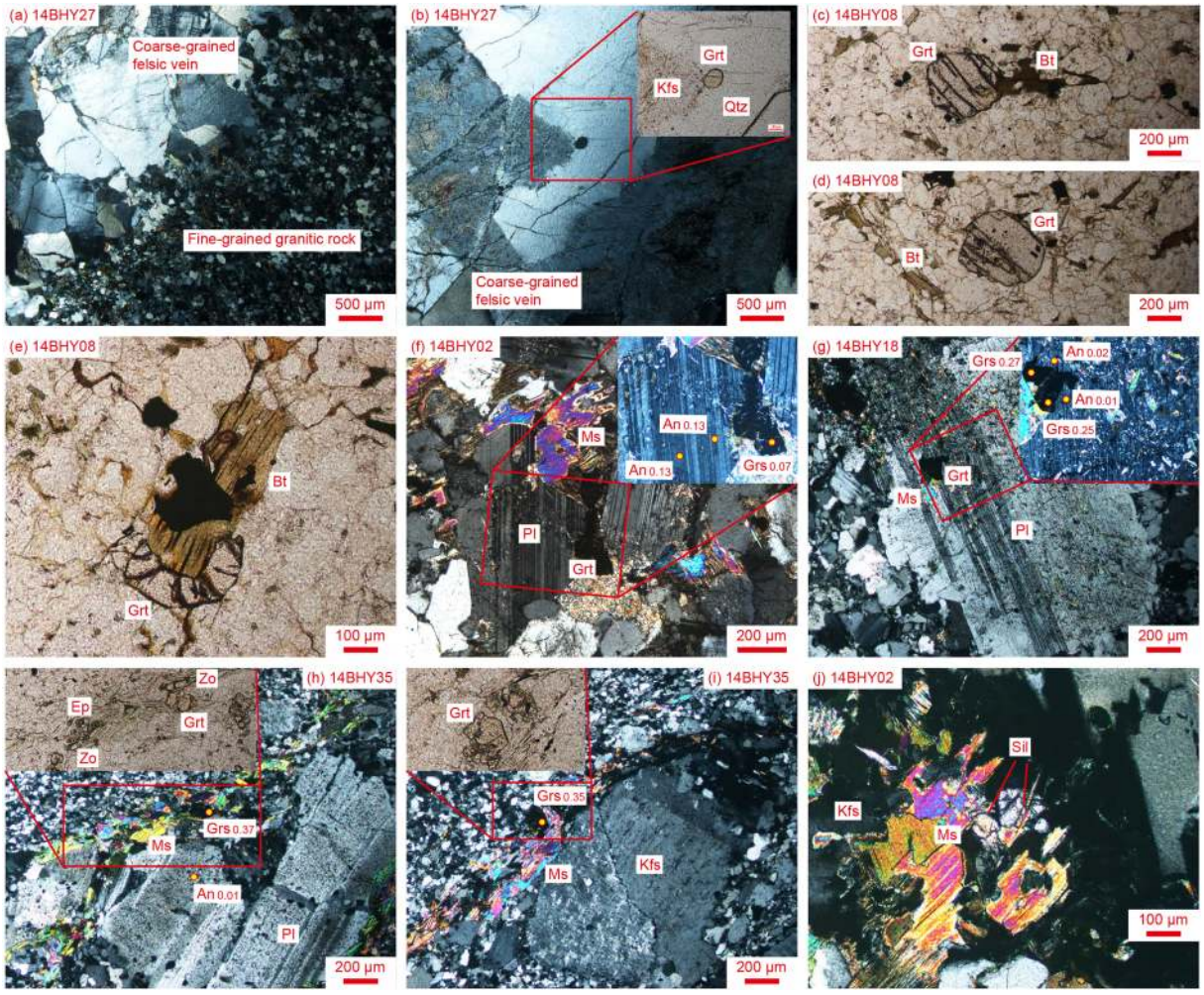

Figure 2. The petrographic textures of metagranites in the Beihuaiyang zone. The grossular contents (Grs) in some garnet grains and anorthite contents (An) in some plagioclase grains based on electron microprobe analyses are also shown. The analysis spots are labelled as yellow circles. (a) Optical microphotograph of fine-grained granitic rock with an inserted coarse-grained felsic vein; (b) a garnet grain in the coarse-grained felsic vein; (c) a garnet grain in coexistence with highly anhedral biotite showing inward penetrating shapes; (d) a garnet grain no longer intergrown with biotite; (e) a garnet corona around anhedral biotite; (f) a garnet grain associated with plagioclase and muscovite, the large plagioclase crystal shows substantial microscopic pores filled by fine-grained muscovite inclusions; (g) a garnet grain and intergrown muscovite included in a large plagioclase crystal which shows more microscopic pores than that in (f); (h) garnet in coexistence with muscovite, plagioclase, epidote, and zoisite. The muscovite is partly aligned along the margin of the large, porous plagioclase crystal; (i) garnet in coexistence with muscovite and K-feldspar. The aligned muscovite grains follow the margin of the K-feldspar large crystal; (j) a sillimanite grain and a sillimanite needle associated with anhedral muscovite showing inward penetrating shapes.

14BHY02 (Figures 2f and 2g). In occasional cases, garnet grains and other Ca-bearing minerals, such as epidote and zoisite, are associated with the aligned muscovite grains along the margin of plagioclase (Figure 2h). The K-feldspar contains almost no muscovite inclusions (Figure 2i). In summary, there are three types of garnet in these metagranite samples. The first one (Garnet-I) occurs in the felsic vein, the second one (Garnet-II) is intergrown with biotite, and the third one (Garnet-III) coexists with muscovite and plagioclase or K-feldspar. In addition, a sillimanite grain and a sillimanite needle are observed in metagranite 14BHY02, coexisting with muscovite which shows inward penetrating shapes (Figure 2j). This texture suggests muscovite dehydration reaction due to temperature increase (He et al., 2018).

In metagranite 07BHY01, all of the three garnet types mentioned above were observed either in thin section or recognized in separated grains according to composition (see section 4.3). In thin section, large (>500 μm) anhedral garnet grains and subhedral to euhedral garnet grains with size around 100 μm were observed (Figure 3a). They are Garnet-II and Garnet-III, respectively. Among the separated grains, most are unzoned (Garnet-II) and rich in quartz inclusions (Figures 3b and 3c). In addition, there are three zoned grains with

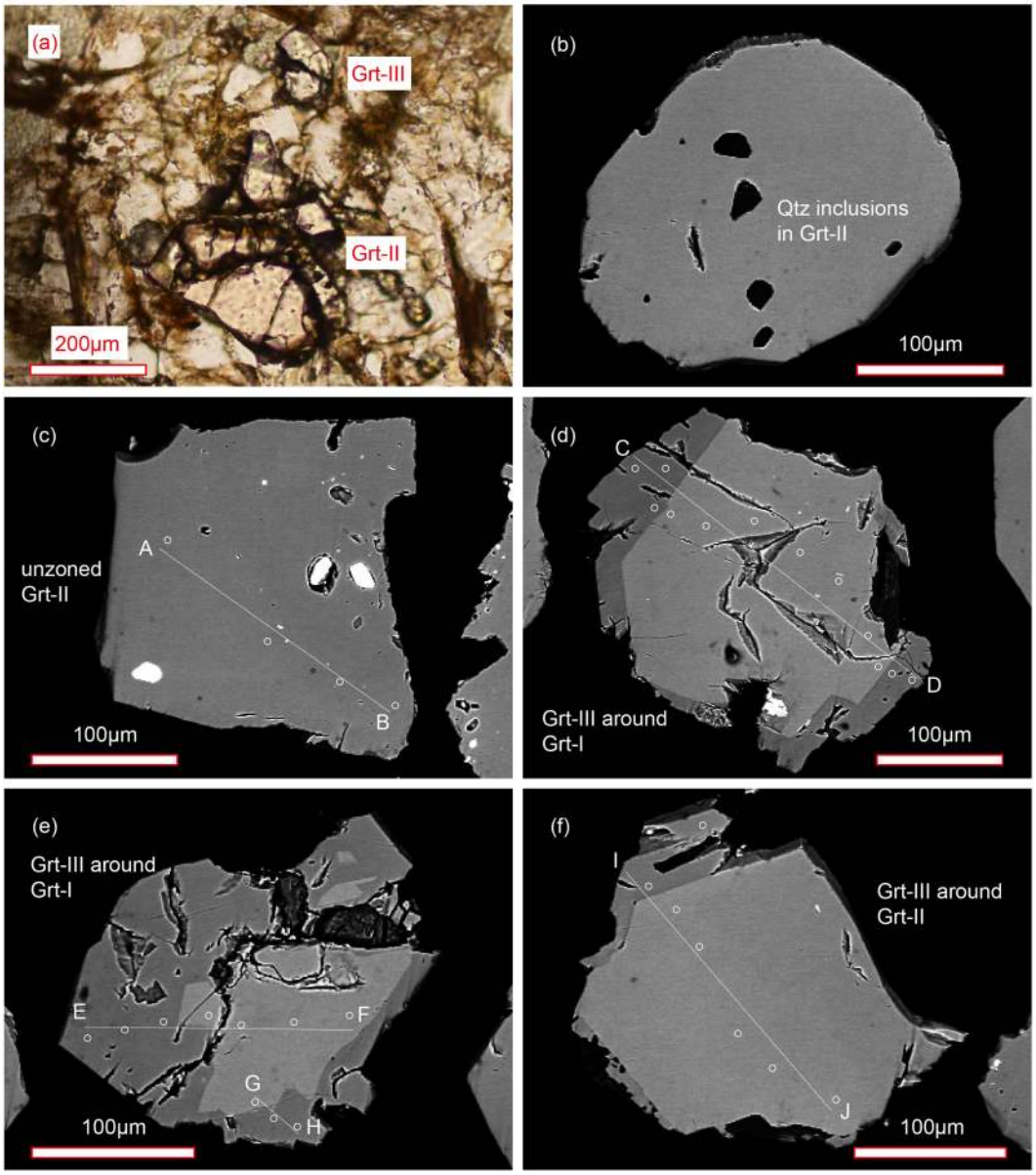

Figure 3. Garnet grains in thin section (a) and mounted in epoxy resin (b–f) from metagranite 07BHY01. The white circles and lines show electron microprobe analysis spots and profiles. (a) Large anhedral and small subhedral to euhedral garnet grains in thin section; (b) a garnet grain rich in quartz inclusions; (c) a garnet grain with homogeneous BSE image; (d–f) garnet grains with compositional zoned BSE images.

the core brighter in BSE images compared with the rim domain (Figures 3d–3f). Two zoned grains (Figures 3d and 3e) have a Mn-rich and Ca-poor core (Garnet-I) surrounded by a 30–50 μm thin rim (Garnet-III). Another zoned grain (Figure 3f) has a core with composition similar to unzoned Garnet-II and is surrounded by a 20–30 μm thin rim (Garnet-III). All the three rims contain higher-Ca and lower-Mn contents, similar to garnet from metagranites 14BHY02, 14BHY18, and 14BHY35.

Based on the petrographic texture and major element composition, the three different types of garnet can be distinguished across the metagranite samples (Table 1). In general, Garnet-I occurs as individual grains in the felsic vein 14BHY27 (Figure 2b) and as cores of two strongly zoned grains in metagranite 07BHY01 (Figures 3d and 3e). Garnet-II is intimately intergrown with biotite in metagranite 14BHY08 (Figures 2c–2e). In metagranite 07BHY01, it occurs as large and anhedral grains in thin section (Figure 3a), unzoned grains (Figures 3b and 3c) and a core of a zoned grain among the separated garnet grains (Figure 3f). Garnet-III coexists with muscovite and plagioclase or K-feldspar in metagranites 14BHY02, 14BHY18 and

Table 1
Summary of Garnet Types in Different Metagranite Samples With Their Petrographic and Geochemical Features Described

Description		Garnet types		
		Garnet-I	Garnet-II	Garnet-III
Corresponding samples		Metagranite 14BHY27 and 07BHY01	Metagranites 14BHY08 and 07BHY01	Metagranites 14BHY02, 14BHY18, 14BHY35 and 07BHY01
Petrographic features	Occurrence	An unzoned grain, cores of two zoned grains	Unzoned grains, a core of a zoned grain	Unzoned grains, rims of zoned grains
	Morphology	Subhedral to euhedral	Anhedral to subhedral	Subhedral to euhedral
	Grain size	100–300 μm	200–500 μm	Grains: 100–200 μm, rims: 20–50 μm
	Intergrown minerals	Quartz and K-feldspar	Biotite	Muscovite and plagioclase or K-feldspar
Geochemical features	Major elements	Mn-rich	Fe- and Mg-rich	Ca-rich
	Trace elements	Positive Eu anomalies, low HREE, moderately high ratios of fluid-mobile to fluid-immobile trace elements	Negative Eu anomalies, high HREE, very low ratios of fluid-mobile to fluid-immobile trace elements	No distinct Eu anomalies, moderate HREE, high ratios of fluid-mobile to fluid-immobile trace elements
	O isotopes	$\delta^{18}O$: −18.1‰ to −16.0‰	$\delta^{18}O$: −17.8‰ to −14.5‰	$\delta^{18}O$: −19.0‰ to −18.3‰

14BHY35 (Figures 2f–2i). In metagranite 07BHY01, it occurs as subhedral to euhedral grains in thin section (Figure 3a) and as rims of the zoned grains among the mounted garnet grains (Figures 3d–3f). It is worth noting that Garnet-III occurs as rims of both Garnet-I and Garnet-II (Figures 3d–3f).

The μXRF scanning of a thin section of metagranite 14BHY08 shows that this rock is composed of 33.0% plagioclase, 26.0% K-feldspar, 24.5% quartz, 4.1% magnetite, 3.7% muscovite, 3.1% biotite, 1.2% garnet, and 0.2% ilmenite (Figure 4).

4.2. Zircon U-Pb Ages and O Isotopes

Zircons in metagranite 07BHY01 are euhedral and elongated with aspect ratios ranging from 1:2 to 1:3. In CL images, they generally show oscillatory zoning without any overgrowth. Some grains exhibit blurred oscillatory zoning or weak CL emission (Figure 5). Zircon U-Pb dating yields $^{206}Pb/^{238}U$ ages varying from

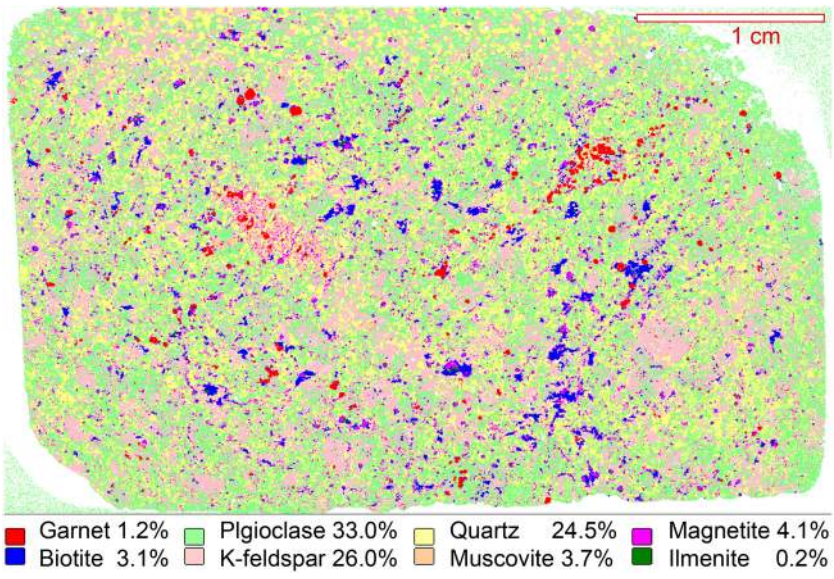

Figure 4. Image of the μXRF scanning on a thin section of metagranite 14BHY08. Mineral proportions are calculated and shown.

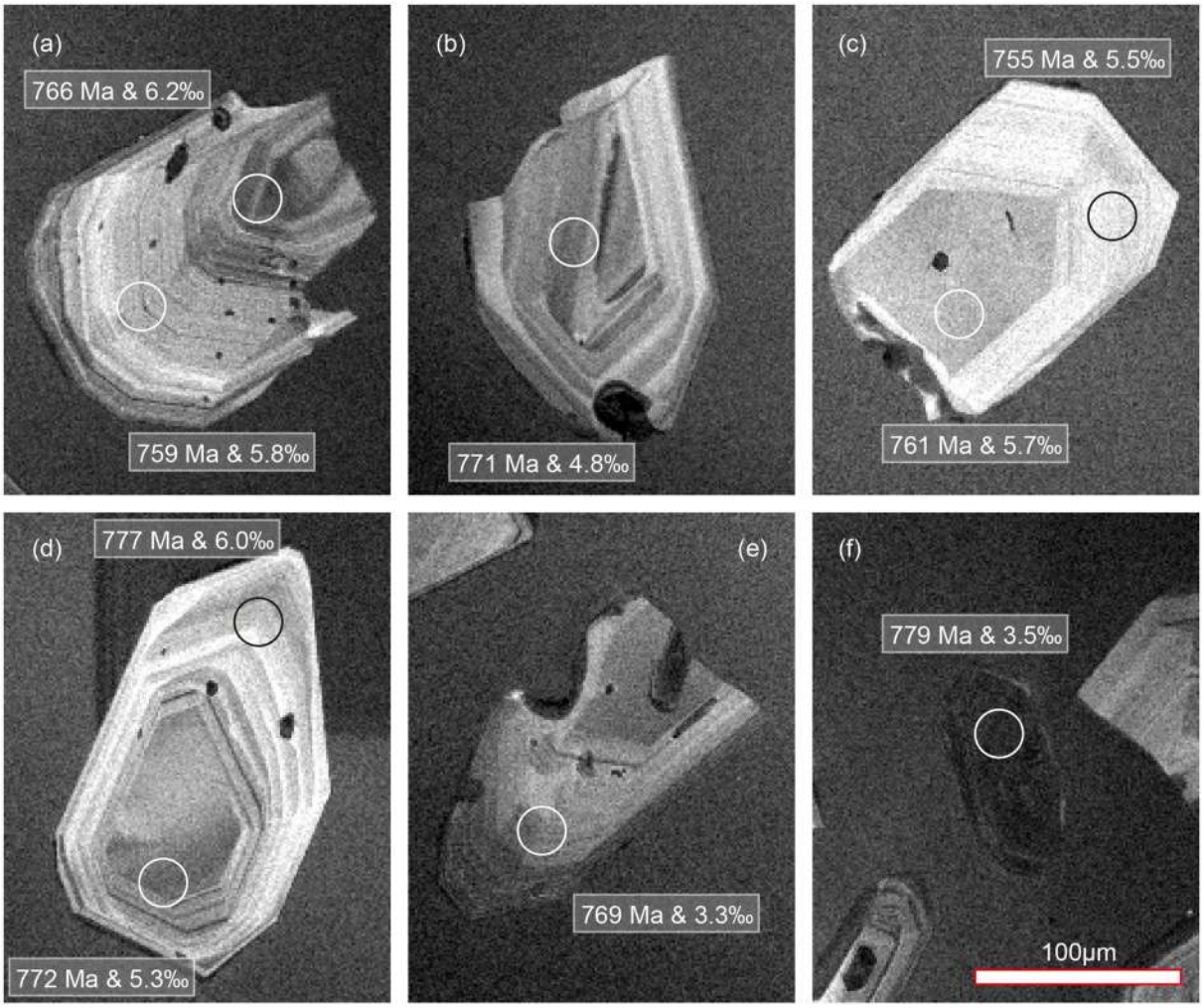

Figure 5. Catahodoluminescence images of zircon from metagranite 07BHY01 with marked the apparent $^{206}Pb/^{238}U$ ages and $\delta^{18}O$ values. (a-d) Zircon grains showing clear oscillatory zoning; (e) a zircon grain showing blurred oscillatory zoning; (f) a zircon grain showing dark CL emission.

647 to 800 Ma (Table 2). A major cluster of dates at 723–782 Ma defines a weighted mean age of 762 ± 6 Ma (n = 37, MSWD = 2.3, Figure 6a).

Zircon $\delta^{18}O$ values vary from 3.3‰ to 6.6‰ (Table 3). The majority of $\delta^{18}O$ values are within the reported value for mantle zircon of 5.3 ± 0.3‰ (Valley et al., 1998), except two lower values of 3.3‰ and 3.5‰ (Figure 6b). The lower $\delta^{18}O$ domains show blurred oscillatory zoning or dark CL emission (Figures 5e and 5f).

4.3. Mineral Geochemistry

The major element composition of garnet from metagranites 07BHY01, 14BHY02, 14BHY18, 14BHY27, and 14BHY35 is listed in supporting information Tables S1 and S2. The garnet and biotite major element compositions of metagranite 14BHY08 are presented in supporting information Table S3 together with the estimated Fe-Mg exchange temperatures. Trace element concentrations of mounted garnet in metagranite 07BHY01 are listed in Table 4. The plagioclase major element composition of metagranites 14BHY02, 14BHY18, and 14BHY35 is presented in supporting information Table S4.

4.3.1. Garnet Major and Trace Element Compositions

The three different garnet types have distinct major element compositions. Representative major element profiles for four mounted garnet grains in metagranite 07BHY01 (Figures 3c–3f) are shown in Figure 7 and the major element results for all the samples are summarized in Figure 8.

Table 2
Zircon SIMS U-Pb Dating Results for Metagranite 07BHY01 From the Beihuaiyang Zone

Analysis No.	Element (ppm)				Measured isotopic ratios						Ages (Ma)					
	Th	U	Pb	Th/U	$^{207}Pb/^{206}Pb$	1σ (%)	$^{207}Pb/^{235}U$	1σ (%)	$^{206}Pb/^{238}U$	1σ (%)	$^{207}Pb/^{206}Pb$	1σ	$^{207}Pb/^{235}U$	1σ	$^{206}Pb/^{238}U$	1σ
S1-01	157	182	31	0.86	0.0647	1.05	1.1266	1.95	0.1262	1.64	766	22	766	11	766	12
S1-02	86	100	17	0.85	0.0649	1.36	1.1184	2.05	0.1250	1.54	771	28	762	11	759	11
S1-03	69	80	13	0.87	0.0650	1.52	1.1415	2.22	0.1274	1.61	774	32	773	12	773	12
S1-04	148	146	25	1.02	0.0637	1.20	1.1156	1.94	0.1270	1.53	732	25	761	10	771	11
S1-05	266	296	51	0.90	0.0645	1.17	1.1462	2.01	0.1288	1.64	759	24	775	11	781	12
S1-07	161	136	24	1.18	0.0652	1.33	1.1231	2.63	0.1250	2.27	779	28	764	14	759	16
S1-08	55	88	14	0.63	0.0644	1.87	1.1038	2.49	0.1242	1.64	756	39	755	13	755	12
S1-09	182	159	28	1.15	0.0646	1.13	1.1157	2.11	0.1253	1.78	761	24	761	11	761	13
S1-10	234	276	47	0.85	0.0642	1.09	1.1271	1.94	0.1273	1.60	748	23	766	10	772	12
S1-11	87	119	20	0.73	0.0653	1.29	1.1411	2.03	0.1267	1.57	784	27	773	11	769	11
S1-12	73	95	16	0.77	0.0629	1.60	1.1124	2.19	0.1283	1.50	703	34	759	12	778	11
S1-13	48	78	12	0.62	0.0638	2.11	1.1264	2.59	0.1281	1.50	734	44	766	14	777	11
S1-14	164	154	27	1.07	0.0668	1.12	1.1720	1.95	0.1272	1.59	832	23	788	11	772	12
S1-15	77	88	15	0.88	0.0659	1.48	1.1704	2.14	0.1289	1.55	802	31	787	12	781	11
S1-16	18	38	6	0.48	0.0665	2.83	1.1525	3.20	0.1257	1.50	822	58	778	18	763	11
S1-17	358	255	48	1.40	0.0651	1.12	1.1249	1.88	0.1254	1.51	776	23	765	10	761	11
S1-19	245	312	51	0.79	0.0654	0.91	1.1275	1.80	0.1250	1.55	788	19	767	10	759	11
S1-20	183	219	37	0.84	0.0658	1.18	1.1616	1.94	0.1281	1.54	799	25	783	11	777	11
S1-21	378	540	88	0.70	0.0656	0.63	1.1613	1.80	0.1284	1.69	794	13	783	10	779	12
S2-01	57	62	11	0.92	0.0671	1.74	1.2226	2.32	0.1321	1.54	841	36	811	13	800	12
S2-02	154	131	23	1.17	0.0655	2.49	1.1103	2.91	0.1229	1.50	790	51	758	16	747	11
S2-03	161	167	29	0.96	0.0640	1.10	1.1174	1.89	0.1267	1.53	740	23	762	10	769	11
S2-05	62	95	15	0.65	0.0663	1.45	1.1442	2.09	0.1253	1.51	814	30	774	11	761	11
S2-06	114	139	22	0.82	0.0645	1.24	1.0710	1.95	0.1205	1.50	757	26	739	10	733	10
S2-07	286	263	47	1.09	0.0656	1.02	1.1499	1.84	0.1271	1.53	795	21	777	10	771	11
S2-08	42	55	9	0.76	0.0677	1.90	1.1230	2.66	0.1204	1.87	858	39	764	14	733	13
S2-09	190	185	33	1.03	0.0653	1.05	1.1564	1.84	0.1285	1.52	783	22	780	10	779	11
S2-10	143	149	25	0.96	0.0674	2.69	1.1224	3.08	0.1208	1.50	850	55	764	17	735	10
S2-11	123	133	22	0.92	0.0663	1.24	1.1253	1.97	0.1231	1.53	816	26	766	11	748	11
S2-12	83	107	17	0.78	0.0632	1.64	1.0602	2.23	0.1217	1.51	715	34	734	12	740	11
S2-14	165	154	27	1.07	0.0641	1.23	1.1276	1.95	0.1275	1.51	746	26	767	11	774	11
S2-15	119	167	23	0.71	0.0637	2.67	0.9273	3.07	0.1056	1.50	730	56	666	15	647	9
S2-16	131	136	23	0.97	0.0662	1.21	1.1125	1.93	0.1218	1.50	814	25	759	10	741	11
S2-17	106	102	18	1.04	0.0663	1.37	1.1725	2.03	0.1283	1.50	815	28	788	11	778	11
S2-18	54	74	12	0.72	0.0654	1.96	1.1276	2.48	0.1250	1.51	787	41	767	13	760	11
S2-19	94	133	20	0.70	0.0642	1.57	1.0647	2.18	0.1203	1.50	747	33	736	11	732	10
S2-20	175	161	26	1.09	0.0637	1.58	1.0425	2.19	0.1187	1.51	732	33	725	11	723	10
S2-22	123	129	22	0.96	0.0637	2.12	1.1317	2.60	0.1289	1.51	731	44	769	14	782	11
S2-23	79	110	18	0.72	0.0642	1.70	1.1353	2.29	0.1284	1.54	747	36	770	12	778	11

Note. S1-01 denotes session 1 analysis number 01.

Garnet-I is rich in Mn with high Sps content of 64–77 mol% and moderate Alm content of 18–30 mol% (Figures 7b and 7c). Garnet-II mainly consists of Alm (39–49 mol%) and Sps (37–53 mol%) components and with a relatively high Prp component (5.7–13 mol%). Both Grs and andradite (Adr) contents are very low (Figure 7a). Garnet-III is characterized by the high Ca contents compared with the other two types (Figures 7b–7d). The grossular component varies from sample to sample with 7.4–12 mol% in metagranite 14BHY02, 23–27 mol% in metagranite 14BHY18, 30–39 mol% in metagranite 14BHY35, and 15–37 mol% in metagranite 07BHY01 (Figure 8). The Sps and Alm contents of Garnet-III are 30–65 mol% and 4.9–33 mol%, respectively.

It should be noted that Garnet-III occurs as rims around Garnet-I in metagranite 07BHY01 (Figures 7b and 7c) and occasionally overgrows Garnet-II (Figure 7d). This means that Garnet-I and Garnet-II are earlier than Garnet-III.

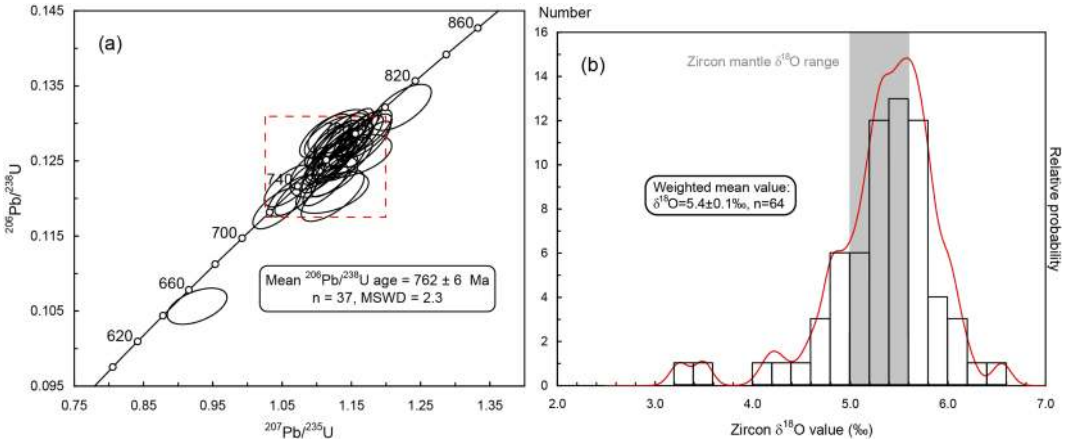

Figure 6. (a) Concordia diagram of zircon U-Pb isotope data for metagranite 07BHY01. Ellipses represent 1σ uncertainties; (b) histogram of zircon $\delta^{18}O$ values for metagranite 07BHY01 with superimposed the relative probability curve (red line). The zircon mantle $\delta^{18}O$ range is shown by the gray rectangle.

The rare earth element (REE) patterns and ratios of fluid-mobile to fluid-immobile trace elements for the three types of garnet are depicted in Figure 9. The REE patterns for Garnet-I are characterized by pronounced positive Eu anomalies and unusually low heavy rare earth element (HREE) concentrations (Figures 9a and 9d). The concentrations of both fluid-immobile trace elements (Sc = 0.5–3.0 ppm, Zr = 0.2–1.8 ppm, and Yb = 0.1–2.1 ppm) and fluid-mobile trace elements (Ba = 0.1–0.4 ppm, Rb = 0.03–0.7 ppm, and Pb = 0.04–0.5 ppm) are relatively low (Table 4). Nevertheless, the ratios of fluid-mobile to fluid-immobile trace elements (i.e., Pb/Zr, Rb/Sc, and Ba/Yb) are moderately high (Figures 9e and 9f). Garnet-II shows more typical patterns, similar to magmatic garnet, with the steeply enriched HREE and significant negative Eu anomalies (Eu/Eu^*_N from 0.04 to 0.39; Figures 9b and 9d). Garnet-II is enriched in the fluid-immobile trace elements (Sc = 68–141 ppm, Zr = 15–22 ppm, and Yb = 18–192 ppm), in contrast to the very low concentrations of fluid-mobile trace elements (Table 4). Therefore, the ratios of fluid-mobile to fluid-

Table 3
SIMS Zircon O Isotopes for Metagranite 07BHY01

O spots	$\delta^{18}O$ (‰)	2σ	O spots	$\delta^{18}O$ (‰)	2σ	O spots	$\delta^{18}O$ (‰)	2σ
S1-01	6.2	0.2	S1-23	4.8	0.2	S2-09	5.3	0.2
S1-02	5.8	0.2	S1-24	5.7	0.3	S2-10	5.3	0.2
S1-03	5.6	0.2	S1-25	5.3	0.3	S2-11	5.5	0.3
S1-04	5.3	0.2	S1-26	6.0	0.2	S2-12	5.5	0.2
S1-05	5.8	0.2	S1-27	5.6	0.2	S2-13	5.3	0.3
S1-06	6.0	0.2	S1-28	5.0	0.3	S2-14	5.5	0.3
S1-07	5.8	0.2	S1-29	3.3	0.2	S2-15	4.8	0.2
S1-08	6.1	0.2	S1-30	5.7	0.3	S2-16	5.6	0.3
S1-09	6.0	0.2	S1-31	5.0	0.2	S2-17	6.6	0.2
S1-10	5.3	0.3	S1-32	5.0	0.2	S2-18	5.5	0.3
S1-11	4.6	0.2	S1-33	5.9	0.2	S2-19	4.5	0.3
S1-12	5.5	0.2	S1-34	3.5	0.2	S2-20	5.5	0.2
S1-13	5.7	0.3	S1-35	4.2	0.2	S2-21	5.2	0.2
S1-14	5.7	0.2	S1-36	5.2	0.3	S2-22	5.2	0.2
S1-15	5.4	0.2	S2-01	5.4	0.3	S2-23	4.9	0.3
S1-16	5.8	0.2	S2-02	5.7	0.2	S2-24	5.1	0.2
S1-17	6.0	0.2	S2-03	5.7	0.2	S2-25	5.3	0.1
S1-18	5.3	0.2	S2-04	5.7	0.2	S2-26	5.6	0.3
S1-19	5.3	0.2	S2-05	5.5	0.2	S2-27	5.4	0.3
S1-20	4.7	0.3	S2-06	5.5	0.3	S2-28	5.1	0.3
S1-21	4.8	0.2	S2-07	5.1	0.2	S2-29	5.1	0.2
S1-22	5.8	0.2	S2-08	5.5	0.2	S2-30	4.3	0.3

Note. S1-01 denotes session 1 analysis number 01.

Table 4
Trace Element Concentrations (ppm) of Mounted Garnet in Metagranite 07BHY01

	Spot											
Element	1-1	1-2	1-3	1-4	2-1	2-2	2-3	2-4	2-5	2-6	2-7	2-8
Type	II	II	II	II	III	III	I	III	I	I	I	III
Li	10.3	5.42	5.88	4.92	0.28	1.67	bdl	1.56	bdl	bdl	bdl	0.91
P	4251	582	607	384	135	134	215	159	281	215	223	83.0
K	148	bdl	1.03	2.53	213	1828	31.4	1227	bdl	5.19	12.7	473
Sc	67.8	126	100	103	1.61	1.66	0.46	2.41	0.73	0.69	1.02	2.70
Ti	130	215	292	292	85.4	99.7	44.6	119	128	19.5	50.4	530
V	11.3	15.1	16.3	16.6	11.3	14.4	2.47	14.1	3.55	2.77	3.62	51.8
Cr	10.4	bdl	10.0	bdl	2.99	bdl	bdl	5.75	bdl	3.26	bdl	bdl
Rb	2.69	0.24	0.13	bdl	1.99	14.6	0.69	9.13	0.03	0.36	0.24	6.80
Sr	3.04	0.02	0.07	bdl	0.10	0.98	0.04	1.31	0.01	0.13	bdl	bdl
Y	175	668	766	692	91.3	89.2	3.07	181	5.05	1.66	1.41	53.3
Zr	17.1	16.1	17.1	16.7	0.07	0.43	0.53	0.72	0.89	0.30	0.22	0.10
Nb	0.24	bdl	0.09	0.03	0.11	0.14	0.11	0.25	0.06	0.05	0.11	0.15
Cs	0.03	bdl	0.01	0.04	0.07	0.14	0.09	0.05	0.11	0.02	bdl	0.38
Ba	0.10	bdl	bdl	0.17	0.52	9.07	0.11	13.1	0.09	bdl	0.35	11.8
La	0.49	0.02	bdl	0.04	0.01	0.03	bdl	0.03	bdl	bdl	bdl	bdl
Ce	4.77	bdl	0.11	0.19	bdl	0.06	0.01	0.14	bdl	0.10	bdl	0.05
Pr	0.89	bdl	0.03	0.01	bdl	0.02	0.04	0.02	0.02	0.02	0.05	0.05
Nd	6.01	0.20	0.11	0.13	0.17	0.24	0.23	0.09	0.37	0.34	0.26	0.20
Sm	4.97	0.33	0.68	0.98	1.16	1.17	0.64	1.26	0.35	0.21	0.33	0.93
Eu	0.82	0.06	0.17	0.16	0.91	0.51	2.38	1.59	2.46	1.61	2.03	0.48
Gd	10.2	7.97	9.17	9.30	5.04	5.09	0.27	6.86	0.32	bdl	bdl	4.18
Tb	3.34	4.27	4.46	4.70	1.32	1.04	0.02	1.88	0.05	0.05	0.04	0.79
Dy	25.7	63.7	74.8	73.6	11.5	9.47	0.38	17.2	1.01	0.35	0.10	4.88
Ho	5.10	21.8	25.5	22.8	2.48	2.23	0.04	4.61	0.16	0.07	0.05	0.86
Er	17.8	114	127	107	6.80	8.39	0.39	16.6	0.70	0.23	0.20	2.29
Tm	2.98	21.4	22.5	18.9	1.21	1.32	0.03	2.07	0.15	bdl	bdl	0.25
Yb	18.4	167	186	145	7.80	8.46	0.70	16.3	1.18	0.16	0.11	1.18
Lu	2.44	30.0	33.7	24.8	1.19	1.69	0.09	2.66	0.13	0.05	0.03	0.18
Hf	0.67	0.34	0.31	0.41	bdl	0.07	bdl	bdl	0.04	bdl	0.04	bdl
Ta	0.10	0.02	0.05	0.01	0.03	bdl	bdl	0.03	bdl	bdl	bdl	0.02
Pb	0.74	0.22	0.09	0.17	0.81	3.09	0.53	4.76	0.04	0.11	0.40	1.58
Th	bdl	bdl	bdl	0.05	bdl	0.03	0.01	bdl	bdl	bdl	bdl	0.04
U	0.24	bdl	0.02	0.03	0.02	0.04	0.20	0.08	0.32	0.33	0.24	bdl

Spot	3-1	3-2	3-3	3-4	3-5	3-6	3-7	4-1	4-2	4-3	4-4
Type	III	III	III	III	I	I	I	III	II	II	II
Li	0.31	2.33	2.19	2.56	0.52	1.31	2.18	6.17	5.70	6.68	8.70
P	252	284	238	210	452	673	552	145	401	402	448
K	4.22	591	181	97.9	10.7	9.51	3.51	27.2	bdl	bdl	4.71
Sc	2.31	4.25	3.24	4.35	1.85	2.64	3.04	124	137	114	141
Ti	189	278	232	130	23.0	28.5	143	894	415	354	193
V	15.5	24.8	26.6	17.9	0.61	1.44	2.48	39.9	20.9	16.2	11.8
Cr	bdl	3.07	2.09	0.30	12.2	1.20	4.64	5.30	1.36	9.96	1.35
Rb	bdl	5.54	1.71	0.42	0.52	0.12	bdl	0.43	0.09	0.33	0.02
Sr	0.23	0.63	0.20	0.15	0.02	bdl	0.01	0.11	0.12	0.07	0.05
Y	16.0	35.9	62.7	137	6.69	16.5	5.95	788	880	889	602
Zr	0.30	1.85	0.89	1.61	1.20	1.76	1.03	0.76	20.8	21.9	14.8
Nb	0.63	0.86	0.95	0.50	0.10	0.10	0.11	1.29	0.04	0.03	0.04
Cs	0.05	0.01	0.05	0.20	0.18	0.02	bdl	0.04	bdl	0.05	bdl
Ba	bdl	1.84	1.89	2.14	0.32	bdl	0.09	1.24	bdl	0.18	bdl
La	bdl	0.03	bdl	0.02	bdl	bdl	bdl	0.08	bdl	bdl	bdl
Ce	0.01	0.12	bdl	0.02	0.04	0.02	bdl	0.04	0.04	bdl	bdl
Pr	0.02	bdl	bdl	bdl	bdl	bdl	bdl	0.05	bdl	0.02	bdl
Nd	0.39	bdl	0.21	0.07	bdl	0.16	0.09	0.09	0.31	0.18	0.11
Sm	0.32	0.16	0.39	1.40	0.10	0.79	0.68	0.55	0.60	1.04	0.21
Eu	0.24	0.95	0.36	0.76	1.54	2.30	1.15	0.72	bdl	0.04	0.15

Table 4
(continued)

Spot	3-1	3-2	3-3	3-4	3-5	3-6	3-7	4-1	4-2	4-3	4-4
Gd	0.63	0.88	1.53	2.77	0.69	0.96	0.73	10.6	11.0	10.7	6.22
Tb	0.10	0.55	0.33	1.14	0.17	0.29	0.10	7.84	5.68	5.36	3.23
Dy	1.39	2.36	3.57	15.0	1.09	1.87	0.95	86.2	79.2	89.0	53.7
Ho	0.40	0.67	1.64	4.20	0.21	0.52	0.18	18.6	28.4	29.1	19.1
Er	1.74	8.42	10.0	21.0	0.83	1.33	0.23	55.0	138	136	97.4
Tm	0.54	2.28	4.23	3.42	0.23	0.25	0.08	7.39	25.5	24.1	19.7
Yb	4.24	30.5	44.4	40.6	1.43	2.10	0.44	45.9	192	184	153
Lu	0.90	7.32	9.08	8.63	0.29	0.29	0.01	5.58	33.0	30.4	27.4
Hf	bdl	bdl	bdl	bdl	bdl	0.04	0.19	0.05	1.05	0.53	0.39
Ta	0.06	0.10	0.05	0.06	bdl	bdl	0.08	0.17	0.02	0.02	0.03
Pb	0.42	2.19	1.03	0.33	0.26	0.18	0.06	2.20	0.13	0.10	0.05
Th	0.10	0.16	0.29	0.08	0.03	0.01	0.03	0.09	0.02	0.01	bdl
U	bdl	0.11	0.04	0.08	0.79	0.72	0.18	0.09	0.11	0.04	0.02

Note. bdl denotes below detection limit.

immobile trace elements are very low (Figures 9e and 9f). Garnet-III has variable HREE concentrations and no distinct Eu anomalies (Figures 9c and 9d). Garnet-III is characterized by relatively high concentrations of fluid-mobile trace elements (Ba = 0.5–13.1 ppm, Rb = 0.4–14.6 ppm, and Pb = 0.3–4.8 ppm) and very low concentrations of fluid-immobile trace elements (Table 4), accounting for the high ratios of fluid-mobile to fluid-immobile trace elements (Figures 9e and 9f).

4.3.2. Biotite and Plagioclase Major Element Compositions

Biotite in metagranite 14BHY08 has Mg# values ranging from 0.39 to 0.51. The MnO and TiO_2 contents are 0.53–1.00 and 1.98–2.79 wt%, respectively. The F content varies from 1.10 to 1.70 wt%.

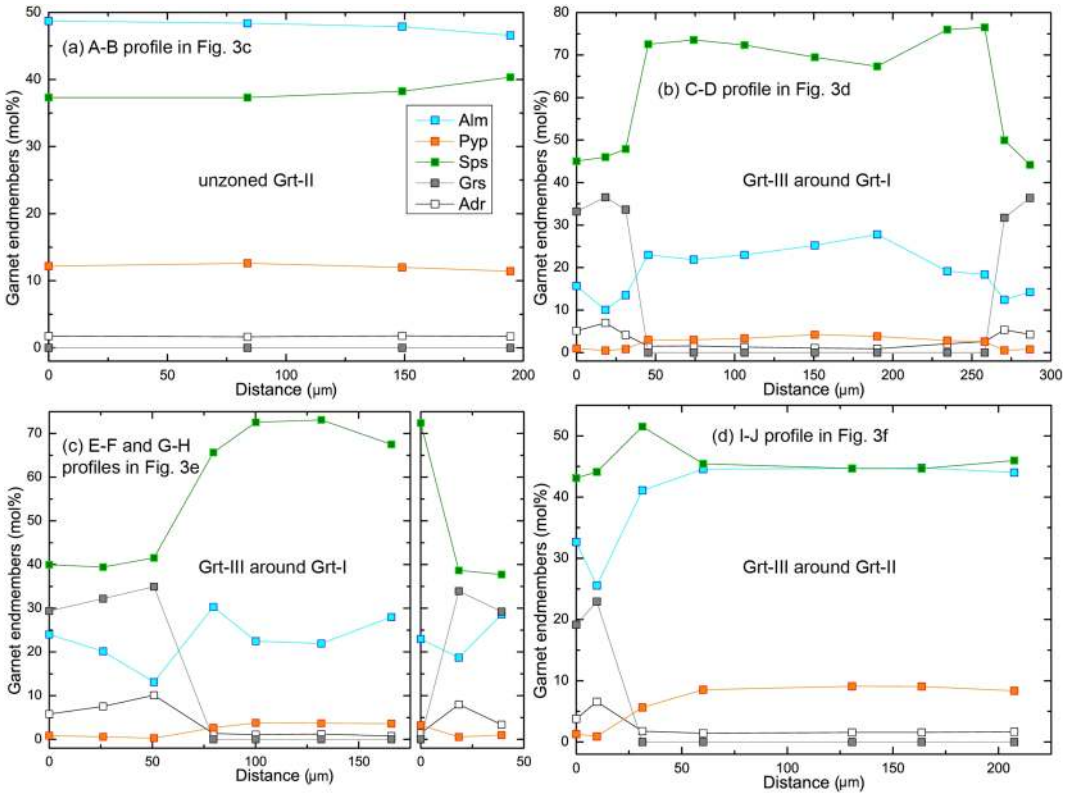

Figure 7. Major element profiles of (a) the homogeneous garnet in Figure 3c and (b–d) zoned garnets in Figures 3d–3f.

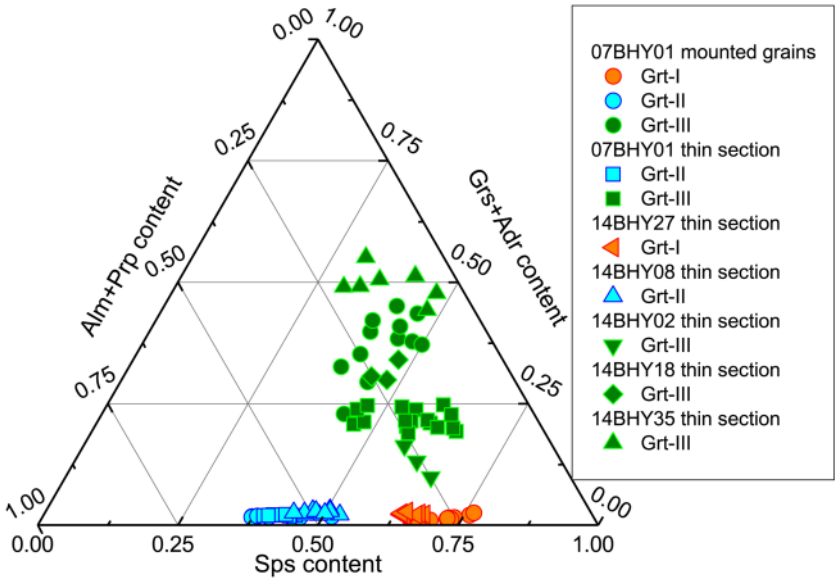

Figure 8. Endmember ternary diagram for three types of garnet in metagranites from the Beihuaiyang zone.

Plagioclase in metagranite 14BHY02 is oligoclase ($Ab_{0.86–0.89}$), and that in metagranite 14BHY18 ($Ab_{0.94–0.98}$) and metagranite 14BHY35 ($Ab_{0.94–0.99}$) is nearly pure albite. A large feldspar crystal in metagranite 14BHY35 has a high Or content of 21 mol%.

4.4. Garnet O Isotopes

The SIMS O isotope analysis results and the garnet composition for the three types of garnet in metagranite 07BHY01 are presented in Tables 5 and 6. The analysis spots are labeled on the BSE images of repolished garnet grains (Figure 10). Garnet $\delta^{18}O$ values show no systematic correlation with endmember chemical components (Figure 11), implying that the matrix effect due to garnet composition was properly corrected. Garnet-I and Garnet-II largely overlap in O isotope composition, with $\delta^{18}O$ values of −18.1‰ to −16.0‰ for

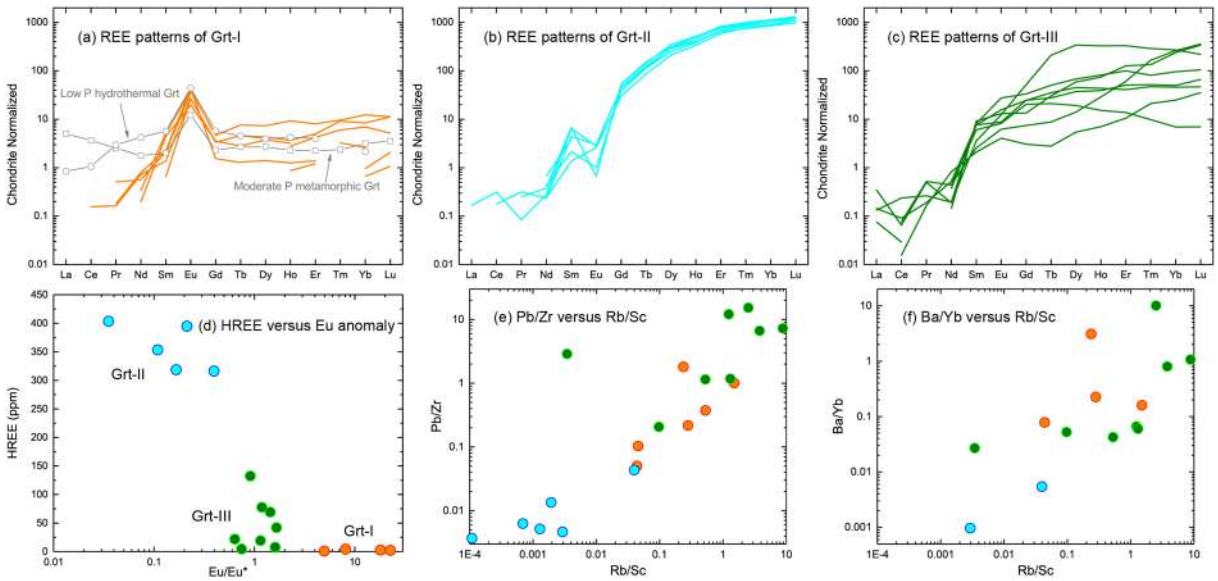

Figure 9. (a–c) Chondrite normalized REE patterns for three types of garnet in metagranite 07BHY01. The REE patterns for low-pressure hydrothermal garnet (Gaspar et al., 2008) and moderate-pressure metamorphic garnet (Hermann & Rubatto, 2003) are also shown. Chondrite REE values are after Sun and McDonough (1989). (d) HREE concentrations versus Eu anomalies. (e) Pb/Zr ratios versus Rb/Sc ratios. (f) Ba/Yb ratios versus Rb/Sc ratios.

Table 5
SIMS Garnet O Isotope Analysis Results for Metagranite 07BHY01, With Endmember Compositions Analyzed by EDS

Analysis NO.	Garnet types	Measured $\delta^{18}O$ (‰)	Error (1σ)	EDS analysis NO.	X_{Prp}	X_{Grs}	X_{Sps}	X_{Alm}	Bias Grs (‰)	Bias Sps (‰)	Corrected $\delta^{18}O$ (‰)	Total error (2σ)
BHY-G1.4C	I	−16.3	0.1	GT1-4-BHY01	0.03	0.02	0.72	0.23	−1.1	2.3	−17.5	0.5
BHY-G1.5C	I	−15.0	0.1	GT1-4-BHY01	0.03	0.02	0.72	0.23	−1.1	2.3	−16.2	0.6
BHY-G1.6C	I	−16.4	0.1	GT1-4-BHY01	0.03	0.02	0.72	0.23	−1.1	2.3	−17.7	0.6
BHY-G2.3C	I	−17.0	0.1	GT2-3-BHY01	0.03	0.01	0.71	0.25	−1.2	2.3	−18.1	0.6
BHY-G2.4C	I	−14.9	0.1	GT2-4-BHY01	0.04	0.01	0.68	0.28	−1.2	2.3	−16.0	0.6
BHY-G2.5C	I	−15.4	0.2	GT2-5-BHY01	0.05	0.01	0.69	0.26	−1.2	2.3	−16.5	0.6
BHY-G2B.1	II	−13.8	0.1	GT2B-BHY01	0.13	0.02	0.35	0.49	−1.1	1.8	−14.5	0.5
BHY-G3.1C	II	−16.6	0.1	GT3-1-BHY01	0.12	0.01	0.38	0.49	−1.2	1.9	−17.3	0.5
BHY-G3.2C	II	−16.6	0.1	GT3-2-BHY01	0.10	0.01	0.41	0.47	−1.2	2.0	−17.5	0.5
BHY-G4.1	II	−15.2	0.2	GT4-1-BHY01	0.11	0.02	0.39	0.48	−1.1	1.9	−16.0	0.6
BHY-G4.2	II	−14.0	0.2	GT4-2-BHY01	0.12	0.02	0.39	0.48	−1.1	1.9	−14.8	0.6
BHY-G5	II	−16.6	0.1	GT4-2-BHY01	0.12	0.02	0.39	0.48	−1.1	1.9	−17.3	0.6
BHY-C1.1	II	−15.5	0.2	C1-1-BHY01	0.10	0.02	0.41	0.47	−1.1	1.9	−16.3	0.6
BHY-C1.2	II	−14.4	0.2	C1-2-BHY01	0.10	0.02	0.41	0.47	−1.1	1.9	−15.2	0.6
BHY-C1.3	II	−15.9	0.1	C1-2-BHY01	0.10	0.02	0.41	0.47	−1.1	1.9	−16.7	0.5
BHY-C3.1	II	−14.1	0.1	C3-1-BHY01	0.08	0.02	0.44	0.46	−1.1	2.0	−15.0	0.5
BHY-C3.2	II	−17.1	0.2	C3-2-BHY01	0.11	0.02	0.38	0.49	−1.1	1.9	−17.8	0.6
BHY-C3.3	II	−14.8	0.1	C3-3-BHY01	0.13	0.02	0.38	0.48	−1.1	1.9	−15.5	0.5
BHY-G1.1	III	−15.0	0.1	GT1-1-BHY01	0.01	0.36	0.41	0.23	1.7	1.9	−18.6	0.5
BHY-G1.3	III	−14.9	0.1	GT1-1-BHY01	0.01	0.36	0.41	0.23	1.7	1.9	−18.5	0.5
BHY-G2.1R	III	−15.2	0.1	GT2-1-BHY01	bdl	0.38	0.37	0.25	1.8	1.8	−18.8	0.5
BHY-G2.2R	III	−14.7	0.1	GT2-1-BHY01	bdl	0.38	0.37	0.25	1.8	1.8	−18.3	0.6
BHY-G3B-1R	III	−15.2	0.1	GT3B-BHY01	0.01	0.39	0.44	0.17	1.8	2.0	−19.0	0.5
BHY-C4.2	III	−15.4	0.1	C4-2-BHY01	0.01	0.26	0.39	0.33	1.1	1.9	−18.4	0.5

Note. bdl denotes below detection limit.

the former and −17.8‰ to −14.5‰ for the latter. Garnet-III has the least variable and marginally lower $\delta^{18}O$ values of −19.0‰ to −18.3‰ (Figures 10 and 11). Notably all these values are at or below the minimum $\delta^{18}O$ value obtained by the laser garnet analysis from the same locality (Zheng et al., 2007), again suggesting the good accuracy for the SIMS analysis. As expected, the SIMS in situ analysis captures some minor components (e.g., Garnet-III) with more extreme values. In contrast, the laser bulk analysis was affected by the relatively ^{18}O-enriched mineral inclusions, such as quartz (Figure 3b) and zircon. The well-preserved Ca zonation in those zoned garnet grains indicates that diffusional resetting of oxygen isotopes is subtle, since oxygen diffusion in garnet is of the same order of magnitude as Ca diffusion (Vielzeuf et al., 2005).

5. Discussion

Since we did not date garnet directly in the present study, a time frame needs to be constructed before discussing the origin of the three types of garnet and connecting their growth to geological evolution according to previously reported zircon and titanite U-Pb ages in the Beihuaiyang zone. Zheng et al. (2007) dated magmatic and hydrothermally altered zircon domains at circa 780 and circa 750 Ma, respectively. In addition, magmatic zircon also records low $\delta^{18}O$ magmatism at circa 750 Ma (Wu et al., 2007). He et al. (2018) report the magmatic zircon of 740–780 Ma and the magmatic titanite of circa 750 Ma. Most importantly, HT/LP metamorphic titanite was dated to grow at circa 750 Ma (He et al., 2018). In summary, there are two major episodes of magmatic activity at circa 780 and circa 750 Ma, respectively. Hydrothermal alteration and HT/LP metamorphism were contemporaneous in the later episode, indicating that circa 750 Ma was the peak stage for the Rodinia breakup6.

In the present study, most zircon grains in metagranite 07BHY01 show clear oscillatory zoning without any later overgrowth (Figure 5). They all have high Th/U ratios of 0.48–1.40 (Table 2), typical of magmatic zircon. U-Pb dating of the magmatic zircon gives ages of 762 ± 6 Ma, consistent with the timing of the

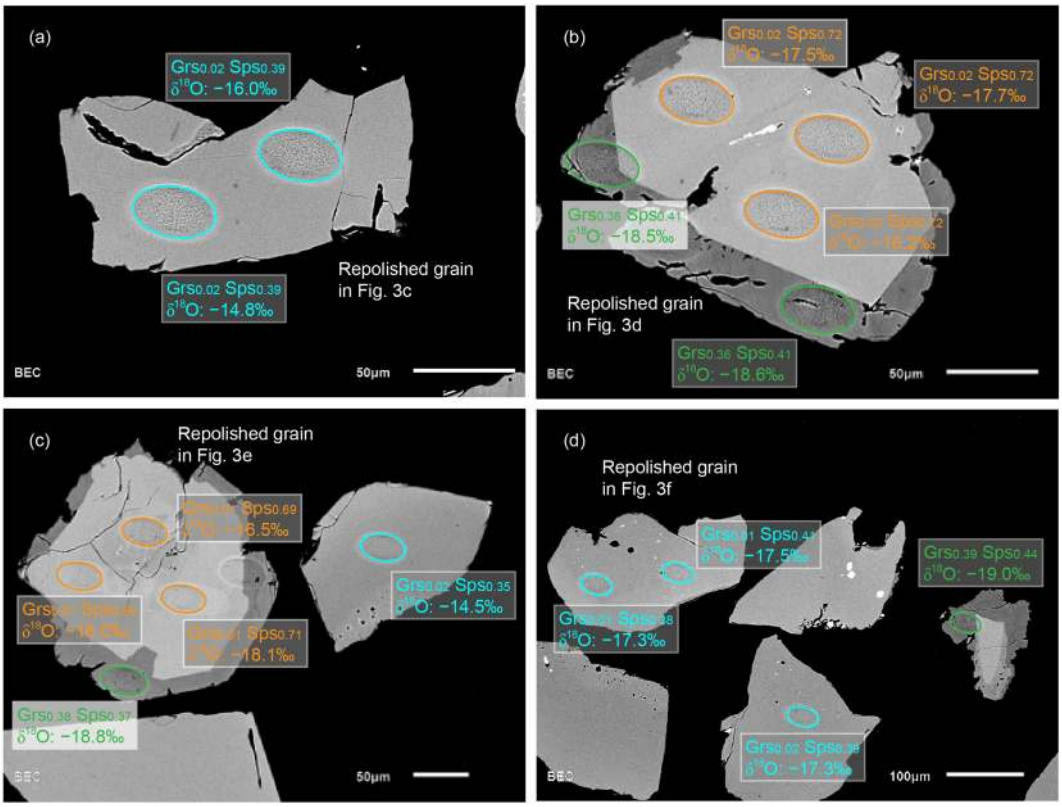

Figure 10. BSE images of garnet grains from metagranite 07BHY01 that were analyzed for O isotopes by SIMS. (a) The repolished garnet grain in Figure 3c; (b) the repolished garnet grain in Figure 3d; (c) the repolished garnet grain in Figure 3e; (d) the repolished garnet grain in Figure 3f. The labeled analysis spots in different garnet zones are distinguished using different colors. Garnet-I: orange, Garnet-II: cyan, Garnet-III: green. For each spot, the Grs and Sps contents and the $\delta^{18}O$ value are shown.

Rodinia breakup (Li, Bogdanova, et al., 2008). In this regard, magmatic zircon records the emplacement of granitic magmas during the continental rifting.

The continental rift setting is further supported by mineral O isotopes. Large scale of ^{18}O depletion over 100,000 km^3 has been recognized along the northern margin of the South China Block, which is ascribed to widespread meteoric water-rock interaction in the continent rift associated with the Rodinia breakup (Zheng et al., 2004). For the metagranites in the Beihuaiyang zone, the previous laser O isotope analysis of mineral separates yields negative $\delta^{18}O$ values as low as −14.4‰ for bulk garnet (Zheng et al., 2007) and −11.7‰ for metamorphic andalusite (He et al., 2018). In the present study, the three types of garnet give even lower $\delta^{18}O$ values of –19.0‰ to −14.5‰. The lowest value provides constraints on the source nature of hydrothermal fluids. Because the O isotope fractionation between water and garnet is as small as 0–3‰ in the range of 200–750 °C (Clayton et al., 1972; Matthews, 1994; Zheng , 1993), a conservative estimation suggests that the hydrothermal fluids should have a $\delta^{18}O$ value as low as −16‰. Among the major terrestrial O isotope reservoirs, meteoric water is the only one known with such negative $\delta^{18}O$ values (Hoefs, 2015). Therefore, meteoric water was a dominant component of the hydrothermal fluids. It is worth noting that the value of −16‰ should be considered as the maximum $\delta^{18}O$ value of the meteoric water because (1) both low $\delta^{18}O$ meteoric water and high $\delta^{18}O$ magmatic water may contribute to hydrothermal systems (Crowe et al., 2001; D'Errico et al., 2012), and (2) meteoric water may evolve to higher $\delta^{18}O$ values than its initial value during the downward penetration along fractures and faults. When comparing with the $\delta^{18}O$ values of modern meteoric water on a global scale, the meteoric water with $\delta^{18}O$ values lower than −16‰ is only found in high latitude regions close to the pole (Bowen & Wilkinson, 2002). However, paleomagnetic studies have revealed that the South China Block in the Middle Neoproterozoic was located at low paleolatitudes (Evans et al., 2000; Yang et al., 2004), where normal meteoric water was unable to achieve such an

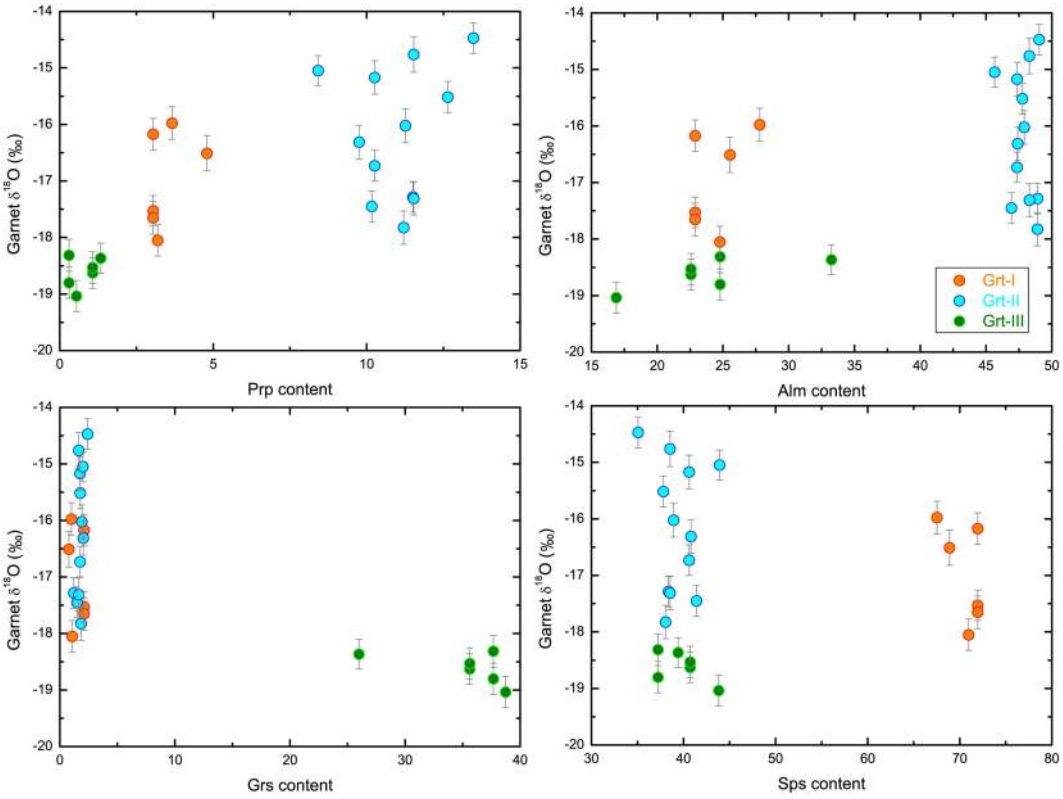

Figure 11. $\delta^{18}O$ values for three garnet types in metagranite 07BHY01 plotted as a function of the four endmember contents. Error bars represent the standard error expressed at 1σ.

extreme ^{18}O depletion (Bowen & Wilkinson, 2002). Therefore, the most likely candidate for the very negative $\delta^{18}O$ fluids is the local continental glacial meltwater (Zheng et al., 2004, 2007).

In contrast to the very negative $\delta^{18}O$ values of garnet, magmatic zircon in the same sample (metagranite 07BHY01) shows mainly mantle-like $\delta^{18}O$ values with only two low values of 3.3‰ and 3.5‰ (Figure 6). Therefore, the magmatic zircon would have crystallized from normal $\delta^{18}O$ magmas prior to pervasive penetration of the continental glacial meltwater. This is further supported by the blurred oscillatory zoning or dark CL image for the two low $\delta^{18}O$ zircon grains (Figure 5), which may be the record of postmagmatic modification by hydrothermal alteration (fluid metasomatism). These grains with dark CL emission have high U concentration and likely high radiogenic damage, making them more susceptible to the fluid metasomatism. Similarly, hydrothermally altered zircons with low $\delta^{18}O$ values of 0.5–2.7‰ from the metagranites in the same locality were reported by Zheng et al. (2007). The scarcity of low $\delta^{18}O$ zircon

Table 6
The Measured $\delta^{18}O$ Values of Standard UWG-2

Analysis NO.	Garnet types	Measured $\delta^{18}O$ (‰)	Total error (2σ)	Note
UWG-1	Standard UWG-2	5.75	0.18	
UWG-2	Standard UWG-2	5.84	0.18	
UWG-3	Standard UWG-2	6.21	0.20	
UWG-4	Standard UWG-2	5.47	0.30	
UWG-5	Standard UWG-2	5.97	0.06	
UWG-6	Standard UWG-2	5.76	0.28	
UWG-7	Standard UWG-2	5.77	0.04	
UWG-8	Standard UWG-2	6.02	0.16	
UWG-9	Standard UWG-2	5.79	0.16	
UWG-10	Standard UWG-2	5.46	0.08	

domains in our samples testifies the limited influence of the fluid metasomatism on the magmatic zircon in the continental rift either during magma emplacement or after magma crystallization (Bindeman et al., 2008; Zheng et al., 2004).

As illustrated above, magmatism, hydrothermal alteration and metamorphism were active at the peak stage of circa 750 Ma for the continental rifting. Because the time intervals between them are within the analytical uncertainties of U-Pb dating, they are contemporaneous in terms of previously reported zircon and titanite U-Pb ages (He et al., 2018; Wu et al., 2007; Zheng et al., 2007). In the present study, their temporal relationships are clarified on the basis of zircon and garnet O isotopes and garnet compositions. Extreme O isotope disequilibrium between the magmatic zircon and the three garnet types indicates that all of the garnet grew under subsolidus conditions after crystallization of the magmatic zircon from the normal $\delta^{18}O$ magmas. In the following subsections, we focus on the processes responsible for the origin of the three episodes of garnets based on their distinct petrographic and geochemical features.

5.1. Garnet-I: Growth During Hydrothermal Alteration

Garnet-I occurs as individual grains in the felsic vein (Figures 2a and 2b) and as the cores of two strongly zoned garnet grains (Figures 3d and 3e). It is mainly composed of Sps and Alm with Sps + Alm > 90 mol %, with Sps contents of 64–77 mol% and Alm contents of 18–30 mol% (Figures 7b and 7c). The very high Sps + Alm contents are similar to the hydrothermal garnet reported by Dziggel et al. (2009). Its REE patterns show pronounced positive Eu anomalies and very low HREE concentrations (Figure 9a), similar to those of hydrothermal garnet in skarns at low pressures (Gaspar et al., 2008) and metamorphic garnet formed from plagioclase breakdown at a moderate pressure of approximately 10 kbar (Hermann & Rubatto, 2003). These studies show that garnet with remarkably different endmember compositions ($Adr_{0.81}Grs_{0.16}$ vs. $Alm_{0.63}Prp_{0.18}Grs_{0.18}$) share similar REE patterns, implying that the garnet REE distribution is not controlled by mineral chemistry. Among other controlling factors in the REE composition of hydrothermal garnet during its growth, fluid chemistry plays a dominant role over growth rate, P-T conditions and oxygen fugacity (Smith et al., 2004). Fluid REE patterns are controlled by temperature and pH rather than rock type (Michard, 1989). Thus, most hydrothermal fluids have REE distribution patterns showing positive Eu anomalies and low HREE concentrations (Klinkhammer et al., 1994). The breakdown of plagioclase supplies enough Eu but insufficient HREE for new garnet growth. Collectively, garnet inherits such REE patterns from the hydrothermal fluids and/or the reactant plagioclase.

It is proposed that Garnet-I with the unusual REE patterns grew during hydrothermal alteration at low pressures, consistent with its very high spessartine contents that extend the garnet stability field to low pressures (Dziggel et al., 2009; Miller & Stoddard, 1981; Symmes & Ferry, 1992). This conclusion is in concordance with the occurrence of Garnet-I in the coarse-grained felsic vein, indicating cocrystallization during the hydrothermal alteration. The hydrothermal origin of Garnet-I is further supported by the moderately high ratios of fluid-mobile to fluid-immobile trace elements (i.e., Rb/Sc, Pb/Zr, and Ba/Yb, Figures 9e and 9f). It is noted that the endmember composition of Garnet-I is distinct from the typical Grs-Adr solid solution for hydrothermal garnet in skarns (Gaspar et al., 2008), which can be explained by various Ca supply during hydrothermal alteration. Skarn garnet reported by Gaspar et al. (2008), was produced when granitic magmas intruded into carbonate-bearing rocks, where the carbonate provided sufficient Ca for the hydrothermal garnet. In contrast, Garnet-I in our study grew when the low-Ca granitic rocks was hydrothermally altered.

Besides the growth of Garnet-I, this episode of hydrothermal alteration was also responsible for the incorporation of the extremely ^{18}O depleted signature into the crustal rocks and the selective alteration on a few zircon domains. They all occurred at the peak stage of the continental rifting. Once the ^{18}O depleted signature was introduced into the rocks, all the products of later processes would inherit the unusual $\delta^{18}O$ value (Zheng et al., 2004, 2007).

5.2. Garnet-II: Growth During Metamorphic Dehydration

Growth of garnet-II is associated with different degrees of biotite decomposition (Figures 2c–2e). Pseudosection calculations were conducted for metagranite 14BHY08 to constrain the metamorphic P-T conditions (Figure 12). Petrographic observations show the presence of minerals such as garnet, biotite, plagioclase, K-feldspar, quartz, secondary muscovite, magnetite, and ilmenite (Figure 4). Subsolidus rather

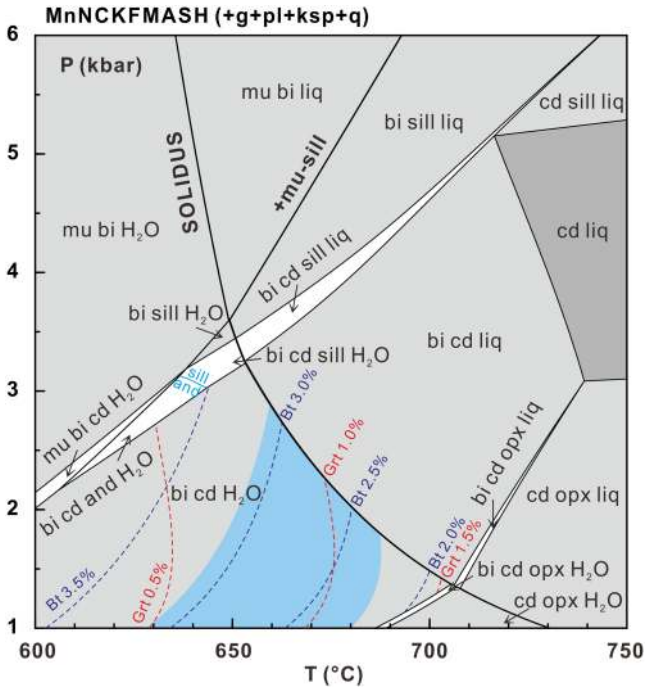

Figure 12. Pseudosection calculations of P-T conditions for metagranite 14BHY08 in MnNCKFMASH system. The red and blue dashed lines represent the mode isopleths of garnet and biotite with the mode values labelled. The light blue area highlights the estimated P-T conditions for the metamorphism based on garnet and biotite contents in the thin section. The depth of shading reflects increased variance, and the darkest fields are quinivariant. Mineral abbreviations: g = garnet; mu = muscovite; bi = biotite; opx = orthopyroxene; cd = cordierite; pl = plagioclase; ksp = K-feldspar; q = quartz; and = andalusite; sill = sillimanite.

than supersolidus conditions are chosen because metamorphic andalusite is stable in metagranite from the same locality (He et al., 2018). In addition, pseudosection calculations based on the andalusite-bearing assemblages by He et al. (2018) reveal that the metamorphism in the sampling area took place at pressures greater than 1.0 kbar. Therefore, the modeled mineral assemblages of garnet, biotite, cordierite, plagioclase, K-feldspar, quartz, and H_2O roughly constrain the P-T region. Although the modeled mineral assemblages contain cordierite, it is not observed in the thin section of metagranite 14BHY08 (Figure 4). This mismatch is likely due to the very low proportions of cordierite as determined by the low whole-rock Fe_2O_3 and MgO contents (He et al., 2018). The mode isopleths of garnet and biotite are then used to further determine the metamorphic P-T conditions. The content of biotite decreases whereas that of garnet increases with temperature increasing (Figure 12), consistent with the petrographic observations (Figures 2c and 2d). The μXRF scanning on the thin section of metagranite 14BHY08 shows that this sample contains 1.2% garnet and 3.1% biotite (Figure 4). The mode isopleths constrain the metamorphism at 1.0–3.0 kbar and 630–690 °C. The estimated P-T conditions are consistent with our earlier results obtained from samples in the same locality (He et al., 2018), both suggesting very high thermal gradients of >60 °C/km at depths of the upper continental crust.

The metamorphic temperatures can be also estimated by the Fe-Mg exchange thermometer between garnet and intergrown biotite (Holdaway, 2000). Assuming a pressure of 2.0 kbar, the thermometry yields temperatures of 608–721 °C (Table S3). A change in the assumed pressure within ±1.0 kbar leads to a change of <6 °C in the calculated temperatures. The estimated temperatures are generally in accordance with those determined by the pseudosection calculations, suggesting that the Fe-Mg equilibrium between garnet and biotite is still preserved. In addition, sillimanite grains and needles consistent with the HT/LP metamorphism are observed in metagranite 14BHY02 (Figure 2i) that was sampled in the same locality as metagranite 14BHY08. Therefore, Garnet-II was produced by metamorphic dehydration through the biotite breakdown at relatively high temperatures.

The chemistry of Garnet-II is also consistent with its metamorphic origin. This type of garnet has high Alm contents (41–49 mol%) and relatively high Prp contents (5.7–13 mol%), resulting from the breakdown of a Fe- and Mg-rich phase such as biotite. Lower than Garnet-I, the Sps contents of Garnet-II are 37–52 mol %, which are high enough for the stabilization of garnet at low pressures (Miller & Stoddard, 1981). Furthermore, Garnet-II has REE patterns with pronounced negative Eu anomalies and high HREE concentrations (Figure 9b). This is in line with growth of K-feldspar during the same metamorphic reaction through biotite breakdown (Hermann & Rubatto, 2003), which is a sink for Eu but does not take up HREE. In addition, Garnet-II has the high concentrations of fluid-immobile trace elements and thus the very low ratios of fluid-mobile to fluid-immobile trace elements (Figures 9e and 9f), supporting its formation through metamorphic dehydration (i.e., the biotite breakdown) rather than hydrothermal alteration (Hickmott et al., 1987).

Similar to the growth of Garnet-II through biotite-breakdown dehydration reaction, metamorphic andalusite produced via muscovite-breakdown dehydration reaction was identified in the same locality (He et al., 2018). The metamorphic andalusite shows a negative $\delta^{18}O$ value of −11.7‰, in contrast to the positive $\delta^{18}O$ values of 4.8‰ to 6.2‰ for magmatic zircon (He et al., 2018). Garnet-II is also in extreme O isotope disequilibrium with the magmatic zircon. In this regard, both metamorphic andalusite and Garnet-II were produced subsequent to cooling and crystallization of the granitic magmas. Elevated temperatures for muscovite and biotite dehydration require a reheating stage, during which metamorphic titanite grew in the metabasalt enclosed by the metagranites (He et al., 2018). The metamorphic titanite U-Pb ages of circa 750 Ma reveal that this episode of metamorphic dehydration took place at the peak stage of the

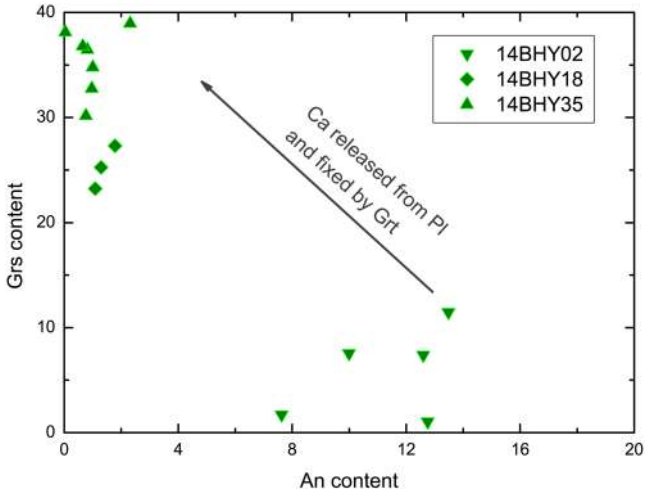

Figure 13. The relationship between the Grs contents of Garnet-III and the An value of coexisting plagioclase in the three investigated samples.

continental rifting (He et al., 2018). Because both garnet and andalusite are refractory minerals that are resistant to later modification (Sharp, 1995; Zheng & Fu, 1998), the negative $\delta^{18}O$ signature of the metamorphic garnet and andalusite must be inherited from the reactant minerals, which had been hydrothermally altered by the continental deglacial meltwater prior to the metamorphic dehydration. In other words, hydrothermal Garnet-I was generated before metamorphic Garnet-II, although the U-Pb ages of hydrothermally altered zircon domains and metamorphic titanite cannot be distinguished from each other within analytical uncertainty (He et al., 2018; Zheng et al., 2007).

5.3. Garnet-III: Growth During Fluid Metasomatism

Plagioclase grains in metagranites 14BHY02, 14BHY18, and 14BHY35 are turbid and porous, containing numerous fine-grained muscovite inclusions (Figures 2f and 2g). This texture is a characteristic feature for interface-coupled dissolution-reprecipitation in fluid metasomatized granites (Putnis & Putnis, 2007). Furthermore, the composition of plagioclases varies from oligoclase ($An_{0.13}$) to nearly pure albite ($An_{0.01}$) with the increasing extent of fluid metasomatism (Figures 2f and 2g), suggesting that the metasomatism would have progressively purged Ca out of the crystal and converted Ca-bearing plagioclase to albite, leading to albitization (Engvik et al., 2008; Kaur et al., 2012; Oliver et al., 2004).

Albitization involves the introduction of Na-rich fluids, providing Na and Si to replace Ca and Al in plagioclase (Oliver et al., 2004). On the one hand, the release of Al is responsible for the growth of muscovite in pores and grain boundaries (Figures 2f–2i). The growth of muscovite during albitization inevitably requires the participation of K. The albitization of K-feldspar (Kaur et al., 2012), which is hinted by its composition of $Ab_{0.79}Or_{0.21}$ (Table S4), could be the source of K. Because no excess Al is released during the albitization of K-feldspar, the K-feldspar grains include almost no fine-grained muscovite (Figure 2i). Alternatively, the external Na-rich fluids could have also contained K.

On the other hand, the release of Ca during albitization of plagioclase resulted in the growth of Ca-bearing minerals such as garnet, epidote, and zoisite (Figures 2f–2h). This episode of fluid metasomatism leads to the formation of Garnet-III, which shows variably high Grs contents of 7.4–39 mol%. Notably, the Grs content of Garnet-III is negatively correlated with the An content of coexisting plagioclase (Figure 13). This indicates that Ca was released from plagioclase and fixed by garnet during the albitization. The release of both Ca and Al is reinforced by the observation that Garnet-III always coexists with muscovite (Figures 2f–2i). As for trace elements, albitization would liberate fluid-mobile Ba, Rb, Pb, and Sr (Baker, 1985; González-Acebrón et al., 2012; Kaur et al., 2012), in agreement with the high Ba, Rb, and Pb concentrations (Table 4) and thus the high ratios of fluid-mobile to fluid-immobile trace elements in Garnet-III (Figures 9e and 9f). Additionally, albitization would not release significant amounts of REE and indeed Garnet-III has overall lower REE contents compared to Garnet-II (Figure 9d). The occasional occurrence of epidote and zoisite would insignificantly influence the REE budget.

The albitization of plagioclase took place subsequent to both hydrothermal alteration and metamorphic dehydration, which is supported by the overgrowth of Garnet-III around both Garnet-I and Garnet-II (Figures 3d–3f). Generally, the albitization of plagioclase takes place under conditions of 350–450 °C and 2–4 kbar (Kaur et al., 2012; Nijland & Touret, 2001). The temperatures are about 250 °C lower than those of the metamorphic dehydration and the pressures are similar, indicating cooling from the peak phase of continental rifting. The Na-rich fluids required for the albitization of plagioclase may be derived from dehydration of the Na-rich, hydrothermally altered, negative $\delta^{18}O$ rocks. Alternatively, more surficial glacial meltwater was added to the albitization fluid. Because the O isotope fractionations between garnet and water are nearly constant at a temperature range from 400 to 700 °C (Zheng, 1993), the second scenario is more plausible because it could explain the systematically lower $\delta^{18}O$ values for metasomatic Garnet-III than hydrothermal Garnet-I (Figure 11). The Na-rich feature of metasomatic fluids is originally related to the hydrothermal alteration of granitic rocks (Bucher & Stober, 2010). This implies that the fractures and

faults that enable the penetrating of negative $\delta^{18}O$ surface water were still well developed and the continental rifting was still active during this episode of fluid activity.

In summary, the magmatic zircon and the three types of garnet record the sequential operation of rift magmatism, hydrothermal alteration, HT/LP metamorphism, and albitization during the continental rifting.

6. Implications for the Identification of Fossil Continental Rifts

Traditionally, basaltic magmatism and basin sedimentation are considered the products of continental rifting (Olsen, 1995; Ruppel, 1995). Our studies indicate that Buchan-type amphibolite to granulite facies metamorphic rocks can be produced by continental rifting at converged plate boundaries (He et al., 2018;Zheng et al., 2019 ; Zheng & Chen, 2017). Thus, Buchan-type metamorphism is also the product of continental rifting (Zheng & Zhao, 2017). Although such metamorphic rocks were frequently superimposed by later geological processes, the operation of hydration and dehydration in these rocks is evident from the geochemistry of refractory minerals. The present study of the metagranites from the Beihuaiyang zone in the Dabie orogen demonstrates that the three types of garnet with distinct features in petrographic textures, major elements, and trace elements are the products of hydrothermal alteration, metamorphic dehydration, and fluid metasomatism, respectively, in the three stages of continental rifting. This provides us with an excellent opportunity to decipher how the hydrothermal system would have evolved in terms of its temperature and water action and how a fossil continental rift can be identified in the metamorphic rocks at the converged plate boundary.

Figure 14 summarizes the formation conditions for the three types of garnet with very negative $\delta^{18}O$ values at the three stages of continental rifting. Garnet-I was produced by the HT hydrothermal alteration, during which the granitic rocks acquired the negative $\delta^{18}O$ signature due to the penetration of continental glacial meltwater (Figure 14a). With continuous thinning of the continental crust and the emplacement of granitic magmas, the crustal temperature would significantly increase for thermal metamorphism, resulting in the expelling of hydrothermal fluids and the breakdown of hydrous minerals (Figure 14b). Because of the metamorphic dehydration, the negative $\delta^{18}O$ signatures were transferred from the hydrothermally altered minerals into Garnet-II (Zheng et al., 2007; this study) and andalusite (He et al., 2018). A similar scenario was proposed for metamorphic zircon with negative $\delta^{18}O$ values as low as −27‰ from the Belomorian complex in Russia (Bindeman et al., 2010) and metamorphic zircon with the lowest $\delta^{18}O$ value of −12‰ in the Sulu orogen of China (He et al., 2016). During the subsequent cooling stage, the hydrothermally altered and metamorphosed granites were metasomatized by the Na-rich fluids to form metasomatic Garnet-III (Figure 14c), with the relatively homogeneous and systematically lower $\delta^{18}O$ values. The presence of magmatic zircon with a pristine magmatic $\delta^{18}O$ values indicates that all the three stages occurred after the crystallization of granitic magmas (Figure 14d).

The constructed evolution history of temperature and fluid action has two important implications for the study of fossil continental rifts.

1. In active continental rifts, lithospheric extension leads to the development of deep fractures and faults (Chapman, 1986; McKenzie, 1978), allowing the surface water (seawater and meteoric water) to penetrate into the crust of 10–15 km depth (Wickham & Taylor, 1987) and to react with the basement rock at high temperature (He et al., 2016; Tang et al., 2008; Zheng et al., 2004, 2007). Because the surface water is significantly depleted in ^{18}O relative to crustal rocks (Hoefs, 2015), HT hydrothermal alteration in continental rifts commonly produces low to negative $\delta^{18}O$ rocks (Solomon & Taylor, 1991; Taylor, 1977, 1990). This process has been verified by a series of case studies in different localities (Bindeman et al., 2010; Bindeman & Serebryakov, 2011; He et al., 2016; Zheng et al., 2004, 2007). One of the main challenges in studying fluid action in fossil continental rifts is to constrain the exact time of surface water penetration. Only a few studies manage to accomplish that by dating contemporaneous products (Zakharov et al., 2017; Zheng et al., 2007). In the present study, mineral O isotopes constrain the penetration of continental deglacial meltwater between the magmatic zircon crystallization and subsequent metamorphism, that is, 760–750 Ma. It works when the two well-dated events are close enough to provide the acceptable results. By doing this, the surface water penetration during continental rifting can provide information on paleoclimate (Zheng et al., 2007;

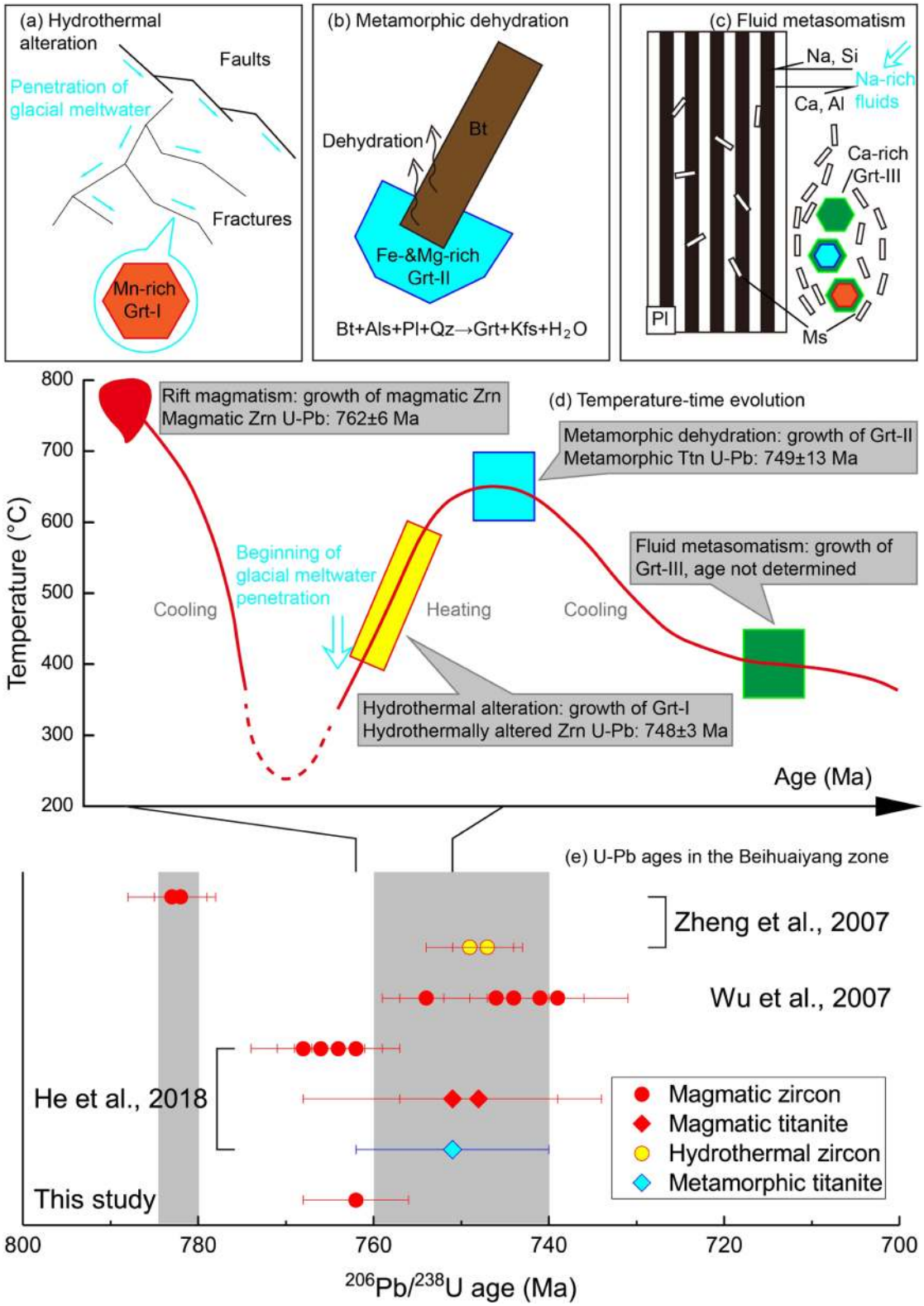

Figure 14. Schematic cartoons illustrating the growth of different types of garnet during continental rifting in the Middle Neoproterozoic. (a) Growth of Garnet-I through hydrothermal alteration with continental glacial meltwater penetrating along fractures and faults, (b) growth of Garnet-II through metamorphic dehydration of biotite, (c) growth of Garnet-III through fluid metasomatism for albitization of plagioclase, and (d) the temperature evolution history from rift magmatism, through hydrothermal alteration, metamorphic dehydration to fluid metasomatism. (e) $^{206}Pb/^{238}U$ ages in zircon and titanite of different origins in the Beihuaiyang zone.

Bindeman et al., 2010; Bindeman & Serebryakov, 2011). For instance, the very negative $\delta^{18}O$ values of Garnet-I require local continental deglacial meltwater at low paleolatitudes, indicating cold paleoclimate in the Middle Neoproterozoic.

2. The presence of Garnet-II testifies the reheating stage for thermal metamorphism, during which high thermal gradients were achieved for the generation of Buchan-type HT/LP metamorphic rocks. Because the substantial influx of energy and matter from the asthenospheric mantle to the lithospheric crust during continental rifting can account for the high thermal gradients at convergent plate boundaries (He et al., 2018; Zheng & Zhao, 2017), the HT/LP metamorphic rocks are able to act as an excellent indicator of fossil continental rifts. The high thermal gradients in continental rifts can be achieved through (1) increased magmatic advective heat transfer from the emplacement of mantle-derived basaltic magmas (Sandiford & Powell, 1986) or large volumes of granitic magmas (Lux et al., 1986), and (2) enhanced conductive heat transfer from the underlying asthenosphere via shallowing of the thermal boundary layer (Houseman et al., 1981; Platt & England, 1994; Zheng & Chen, 2017). In the present case in the Beihuaiyang zone, the HT/LP metamorphism was contemporaneous with the second episode of rift magmatism at a regional scale (Figure 14e). In this regard, the coeval magmatism and metamorphism are two aspects reflecting high heat flow in the continental rift. In addition, the asthenospheric mantle may undergo decompressional melting during the continental rifting, giving rise to basaltic melts with high heat amounts. As a consequence, magma emplacement can also enhance the upward heat transfer and increase the thermal gradients at the depth of the upper continental crust. Therefore, the HT/LP metamorphic rocks are the product of continental rifting (He et al., 2018), similar to HT to ultrahigh-temperature granulite-facies metamorphic rocks (Zheng et al., 2019; Zheng & Chen, 2017). These rocks preserve the P-T-t information of crustal rocks during the rift metamorphism, complementary to rift magmatic rocks.

7. Conclusions

The microscale chemical and O isotopic compositions of refractory minerals in the metagranites from the northern margin of the South China Block reveals the operation of hydration and dehydration during continental rifting at the converged plate boundary. Magmatic zircon with mantle-like O isotope compositions records the crystallization of granitic magmas prior to penetration of the negative $\delta^{18}O$ fluids. Three types of garnet with negative $\delta^{18}O$ values were produced by hydrothermal alteration, metamorphic dehydration, and fluid metasomatism, respectively, during the successful continental rifting in response to the Rodinia breakup. All of the garnet types are postmagmatic products, and they record different stages of the continental rifting. The negative $\delta^{18}O$ values of Garnet-I indicate the infiltration of continental deglacial meltwater in an active rift setting. The negative $\delta^{18}O$ signature was then transferred into metamorphic Garnet-II through biotite breakdown at the reheating stage. Pseudosection calculations indicate that the metamorphic dehydration took place at 1.0–3.0 kbar and 630–690 °C, corresponding to very high thermal gradients of >60 °C/km. Therefore, the HT/LP metamorphic rocks are an excellent indicator of the continental rifting. The later growth of metasomatic Garnet-III requires contributions from Na-rich fluids liberated from the previously altered and metamorphosed rocks. Addition of the negative $\delta^{18}O$ surface water is also required. The garnet geochemistry records a series of geological processes under subsolidus conditions during the continental rifting in response to the Rodinia breakup.

Acknowledgments
This study was supported by funds from the National Natural Science Foundation of China (41590624 and 41572168). Thanks are due to Yi-Xiang Chen and Wei Rong for their assistance with the field trip, to Xian-Hua Li and Qiu-Li Li for zircon SIMS analyses, and to Gui-Bing Zhang for assistance with in situ garnet O isotope analysis. Comments by Ilya Bindeman and Ethan Baxter are very helpful for improvement of the presentation. The data for the present study are archived at Mendeley Data (https://data.mendeley.com/datasets/2kf3nvt83z/1).

References

Baker, J. H. (1985). Rare-earth and other trace-element mobility accompanying albitization in a Proterozoic granite, West-Bergslagen, Sweden. *Mineralogical Magazine*, *49*(350), 107–115. https://doi.org/10.1180/minmag.1985.049.350.17

Baxter, E. F., & Caddick, M. J. (2013). Garnet growth as a proxy for progressive subduction zone dehydration. *Geology*, *41*(6), 643–646. https://doi.org/10.1130/G34004.1

Baxter, E. F., Caddick, M. J., & Ague, J. J. (2013). Garnet: Common mineral, uncommonly useful. *Elements*, *9*(6), 415–419. https://doi.org/10.2113/gselements.9.6.415

Baxter, E. F., Caddick, M. J., & Dragovic, B. (2017). Garnet: A rock-forming mineral petrochronometer. *Reviews in Mineralogy and Geochemistry*, *83*(1), 469–533. https://doi.org/10.2138/rmg.2017.83.15

Baxter, E. F., & Scherer, E. E. (2013). Garnet geochronology: Timekeeper of tectonometamorphic processes. *Elements*, *9*(6), 433–438. https://doi.org/10.2113/gselements.9.6.433

Bertotti, G., Siletto, G. B., & Spalla, M. I. (1993). Deformation and metamorphism associated with crustal rifting: The Permian to Liassic evolution of the Lake Lugano-Lake Como area (Southern Alps). *Tectonophysics*, *226*(1-4), 271–284. https://doi.org/10.1016/0040-1951(93)90122-Z

Bindeman, I. N., Brooks, C. K., McBirney, A. R., & Taylor, H. P. (2008). The low-$\delta^{18}O$ late-stage ferrodiorite magmas in the Skaergaard intrusion: Result of liquid immiscibility, thermal metamorphism, or meteoric water incorporation into magma? *Journal of Geology*, *116*(6), 571–586. https://doi.org/10.1086/591992

Bindeman, I. N., Schmitt, A. K., & Evans, D. A. D. (2010). Limits of hydrosphere-lithosphere interaction: Origin of the lowest-known $\delta^{18}O$ silicate rock on Earth in the Paleoproterozoic Karelian rift. *Geology*, *38*(7), 631–634. https://doi.org/10.1130/G30968.1

Bindeman, I. N., & Serebryakov, N. S. (2011). Geology, petrology and O and H isotope geochemistry of remarkably ^{18}O depleted Paleoproterozoic rocks of the Belomorian Belt, Karelia, Russia, attributed to global glaciation 2.4 Ga. *Earth and Planetary Science Letters*, *306*(3), 163–174. https://doi.org/10.1016/j.epsl.2011.03.031

Bindeman, I. N., & Valley, J. W. (2000). Formation of low-$\delta^{18}O$ rhyolites after caldera collapse at Yellowstone, Wyoming, USA. *Geology*, *28*(8), 719–722. https://doi.org/10.1130/0091-7613(2000)28<719:FOLRAC>2.0.CO;2

Bowen, G. J., & Wilkinson, B. (2002). Spatial distribution of $\delta^{18}O$ in meteoric precipitation. *Geology*, *30*(4), 315–318. https://doi.org/10.1130/0091-7613(2002)030<0315:SDOOIM>2.0.CO;2

Bucher, K., & Stober, I. (2010). Fluids in the upper continental crust. *Geofluids*, *10*(1–2), 241–253. https://doi.org/10.1111/j.1468-8123.2010.00279.x

Buck, W. R. (2015). The dynamics of continental breakup and extension. *Treatise on Geophysics*, *6*, 325–379.

Chamberlain, C. P., & Conrad, M. E. (1991). Oxygen isotope zoning in garnet. *Science*, *254*(5030), 403–406. https://doi.org/10.1126/science.254.5030.403

Chapman, D. (1986). Thermal gradients in the continental crust. *Geological Society of London, Special Publication*, *24*(1), 63–70. https://doi.org/10.1144/GSL.SP.1986.024.01.07

Chen, F., Guo, J.-H., Jiang, L.-L., Siebel, W., Cong, B., & Satir, M. (2003). Provenance of the Beihuaiyang lower-grade metamorphic zone of the Dabie ultrahigh-pressure collisional orogen, China: Evidence from zircon ages. *Journal of Asian Earth Sciences*, *22*(4), 343–352. https://doi.org/10.1016/S1367-9120(03)00068-3

Clayton, R. N., O'Neil, J. R., & Mayeda, T. K. (1972). Oxygen isotope exchange between quartz and water. *Journal of Geophysical Research*, *77*(17), 3057–3067. https://doi.org/10.1029/JB077i017p03057

Cloetingh, S., & Wortel, R. (1986). Stress in the Indo-Australian plate. *Tectonophysics*, *132*, 49–67. https://doi.org/10.1016/0040-1951(86)90024-7

Coggon, R., & Holland, T. J. B. (2002). Mixing properties of phengitic micas and revised garnet-phengite thermobarometers. *Journal of Metamorphic Geology*, *20*(7), 683–696. https://doi.org/10.1046/j.1525-1314.2002.00395.x

Crowe, D. E., Riciputi, L. R., Bezenek, S., & Ignatiev, A. (2001). Oxygen isotope and trace element zoning in hydrothermal garnets: Windows into large-scale fluid-flow behavior. *Geology*, *29*(6), 479–482. https://doi.org/10.1130/0091-7613(2001)029<0479:OIATEZ>2.0.CO;2

D'Errico, M. E., Lackey, J. S., Surpless, B. E., Loewy, S. L., Wooden, J. L., Barnes, J. D., et al. (2012). A detailed record of shallow hydrothermal fluid flow in the Sierra Nevada magmatic arc from low-$\delta^{18}O$ skarn garnets. *Geology*, *40*(8), 763–766. https://doi.org/10.1130/G33008.1

Dewey, J. F., & Burke, K. (1974). Hot spots and continental break-up: Implications for collisional orogeny. *Geology*, *2*(2), 57–60. https://doi.org/10.1130/0091-7613(1974)2<57:HSACBI>2.0.CO;2

Dragovic, B., Baxter, E. F., & Caddick, M. J. (2015). Pulsed dehydration and garnet growth during subduction revealed by zoned garnet geochronology and thermodynamic modeling, Sifnos, Greece. *Earth and Planetary Science Letters*, *413*, 111–122. https://doi.org/10.1016/j.epsl.2014.12.024

Dziggel, A., Wulff, K., Kolb, J., Meyer, F. M., & Lahaye, Y. (2009). Significance of oscillatory and bell-shaped growth zoning in hydrothermal garnet: Evidence from the Navachab gold deposit, Namibia. *Chemical Geology*, *262*(3–4), 262–276. https://doi.org/10.1016/j.chemgeo.2009.01.027

Engvik, A. K., Putnis, A., Fitz Gerald, J. D., & Austrheim, H. (2008). Albitization of granitic rocks: The mechanism of replacement of oligoclase by albite. *The Canadian Mineralogist*, *46*(6), 1401–1415. https://doi.org/10.3749/canmin.46.6.1401

Ernst, W. G., Tsujimori, T., Zhang, R., & Liou, J. G. (2007). Permo-Triassic collision, subduction-zone metamorphism, and tectonic exhumation along the east Asian continental margin. *Annual Review of Earth and Planetary Sciences*, *35*(1), 73–110. https://doi.org/10.1146/annurev.earth.35.031306.140146

Evans, D. A. D., Li, Z. X., Kirschvink, J. L., & Wingate, M. T. D. (2000). A high-quality mid-Neoproterozoic paleomagnetic pole from South China, with implications for ice ages and the breakup configuration of Rodinia. *Precambrian Research*, *100*(1–3), 313–334. https://doi.org/10.1016/S0301-9268(99)00079-0

Fu, B., Kita, N. T., Wilde, S. A., Liu, X., Cliff, J., & Greig, A. (2013). Origin of the Tongbai-Dabie-Sulu Neoproterozoic low-$\delta^{18}O$ igneous province, east-central China. *Contributions to Mineralogy and Petrology*, *165*(4), 641–662. https://doi.org/10.1007/s00410-012-0828-3

Gaspar, M., Knaack, C., Meinert, L. D., & Moretti, R. (2008). REE in skarn systems: A LA-ICP-MS study of garnets from the Crown Jewel gold deposit. *Geochimica et Cosmochimica Acta*, *72*(1), 185–205. https://doi.org/10.1016/j.gca.2007.09.033

Giese, U., & Bühn, B. (1994). Early Paleozoic rifting and bimodal volcanism in the Ossa-Morena Zone of south-west Spain. *Geologische Rundschau*, *83*(1), 143–160. https://doi.org/10.1007/BF00211898

González-Acebrón, L., Götze, J., Barca, D., Arribas, J., Mas, R., & Pérez-Garrido, C. (2012). Diagenetic albitization in the Tera Group, Cameros Basin (NE Spain) recorded by trace elements and spectral cathodoluminescence. *Chemical Geology*, *312–313*, 148–162. https://doi.org/10.1016/j.chemgeo.2012.04.012

Hacker, B. R., Ratschbacher, L., Webb, L., Ireland, T., Walker, D., & Shuwen, D. (1998). U/Pb zircon ages constrain the architecture of the ultrahigh-pressure Qinling–Dabie Orogen, China. *Earth and Planetary Science Letters*, *161*(1–4), 215–230. https://doi.org/10.1016/S0012-821X(98)00152-6

He, Q., Zhang, S.-B., & Zheng, Y.-F. (2016). High temperature glacial meltwater–rock reaction in the Neoproterozoic: Evidence from zircon in-situ oxygen isotopes in granitic gneiss from the Sulu orogen. *Precambrian Research*, *284*, 1–13. https://doi.org/10.1016/j.precamres.2016.07.012

He, Q., Zhang, S.-B., & Zheng, Y.-F. (2018). Evidence for regional metamorphism in a continental rift during the Rodinia breakup. *Precambrian Research*, *314*, 414–427. https://doi.org/10.1016/j.precamres.2018.06.009

Hermann, J., & Rubatto, D. (2003). Relating zircon and monazite domains to garnet growth zones: Age and duration of granulite facies metamorphism in the Val Malenco lower crust. *Journal of Metamorphic Geology*, *21*(9), 833–852. https://doi.org/10.1046/j.1525-1314.2003.00484.x

Hickmott, D. D., Shimizu, N., Spear, F. S., & Selverstone, J. (1987). Trace-element zoning in a metamorphic garnet. *Geology*, *15*(6), 573–576. https://doi.org/10.1130/0091-7613(1987)15<573:TZIAMG>2.0.CO;2

Hoefs, J. (2015). *Stable isotope geochemistry* (7th ed.). Switzerland: Springer International Publishing.
Holdaway, M. J. (2000). Application of new experimental and garnet Margules data to the garnet-biotite geothermometer. *American Mineralogist*, *85*(7-8), 881–892. https://doi.org/10.2138/am-2000-0701
Holland, T., & Powell, R. (2003). Activity–composition relations for phases in petrological calculations: An asymmetric multicomponent formulation. *Contributions to Mineralogy and Petrology*, *145*(4), 492–501. https://doi.org/10.1007/s00410-003-0464-z
Holland, T. J. B., & Powell, R. (1998). An internally consistent thermodynamic data set for phases of petrological interest. *Journal of Metamorphic Geology*, *16*(3), 309–343. https://doi.org/10.1111/j.1525-1314.1998.00140.x
Houseman, G. A., McKenzie, D. P., & Molnar, P. (1981). Convective instability of a thickened boundary layer and its relevance for the thermal evolution of continental convergent belts. *Journal of Geophysical Research*, *86*(B7), 6115–6132. https://doi.org/10.1029/JB086iB07p06115
Ickert, R. B., & Stern, R. A. (2013). Matrix corrections and error analysis in high-precision SIMS $^{18}O/^{16}O$ measurements of Ca–Mg–Fe garnet. *Geostandards and Geoanalytical Research*, *37*(4), 429–448. https://doi.org/10.1111/j.1751-908X.2013.00222.x
Jamtveit, B., Wogelius, R. A., & Fraser, D. G. (1993). Zonation patterns of skarn garnets: Records of hydrothermal system evolution. *Geology*, *21*(2), 113–116. https://doi.org/10.1130/0091-7613(1993)021<0113:ZPOSGR>2.3.CO;2
Kaur, P., Chaudhri, N., Hofmann, A. W., Raczek, I., Okrusch, M., Skora, S., & Baumgartner, L. P. (2012). Two-stage, extreme albitization of A-type granites from Rajasthan, NW India. *Journal of Petrology*, *53*(5), 919–948. https://doi.org/10.1093/petrology/egs003
King, E. M., Tucker Barrie, C., & Valley, J. W. (1997). Hydrothermal alteration of oxygen isotope ratios in quartz phenocrysts, Kidd Creek mine, Ontario: Magmatic values are preserved in zircon. *Geology*, *25*(12), 1079–1082. https://doi.org/10.1130/0091-7613(1997)025<1079:HAOOIR>2.3.CO;2
Klinkhammer, G. P., Elderfield, H., Edmond, J. M., & Mitra, A. (1994). Geochemical implications of rare earth element patterns in hydrothermal fluids from mid-ocean ridges. *Geochimica et Cosmochimica Acta*, *58*(23), 5105–5113. https://doi.org/10.1016/0016-7037(94)90297-6
Lackey, J. S., Erdmann, S., Hark, J. S., Nowak, R. M., Murray, K. E., Clarke, D. B., & Valley, J. W. (2011). Tracing garnet origins in granitoid rocks by oxygen isotope analysis: Examples from the South Mountain Batholith, Nova Scotia. *The Canadian Mineralogist*, *49*(2), 417–439. https://doi.org/10.3749/canmin.49.2.417
Le Breton, N., & Thompson, A. B. (1988). Fluid-absent (dehydration) melting of biotite in metapelites in the early stages of crustal anatexis. *Contributions to Mineralogy and Petrology*, *99*(2), 226–237. https://doi.org/10.1007/BF00371463
Li, X.-H., Li, W.-X., Li, Q.-L., Wang, X.-C., Liu, Y., & Yang, Y.-H. (2010). Petrogenesis and tectonic significance of the ~850 Ma Gangbian alkaline complex in South China: Evidence from in situ zircon U–Pb dating, Hf–O isotopes and whole-rock geochemistry. *Lithos*, *114*(1–2), 1–15. https://doi.org/10.1016/j.lithos.2009.07.011
Li, X.-H., Li, W.-X., Li, Z.-X., & Liu, Y. (2008). 850–790 Ma bimodal volcanic and intrusive rocks in northern Zhejiang, South China: A major episode of continental rift magmatism during the breakup of Rodinia. *Lithos*, *102*(1), 341–357. https://doi.org/10.1016/j.lithos.2007.04.007
Li, X.-H., Li, Z.-X., Zhou, H., Liu, Y., & Kinny, P. D. (2002). U–Pb zircon geochronology, geochemistry and Nd isotopic study of Neoproterozoic bimodal volcanic rocks in the Kangdian Rift of South China: Implications for the initial rifting of Rodinia. *Precambrian Research*, *113*(1), 135–154. https://doi.org/10.1016/S0301-9268(01)00207-8
Li, X. H., Liu, Y., Li, Q. L., Guo, C. H., & Chamberlain, K. R. (2009). Precise determination of Phanerozoic zircon Pb/Pb age by multicollector SIMS without external standardization. *Geochemistry, Geophysics, Geosystems*, *10*, Q04010. https://doi.org/10.1029/2009GC002400
Li, X. H., Long, W. G., Li, Q. L., Liu, Y., Zheng, Y. F., Yang, Y. H., et al. (2010). Penglai zircon megacrysts: A potential new working reference material for microbeam determination of Hf-O isotopes and U-Pb age. *Geostandards and Geoanalytical Research*, *34*(2), 117–134. https://doi.org/10.1111/j.1751-908X.2010.00036.x
Li, Z.-X., Bogdanova, S., Collins, A., Davidson, A., De Waele, B., Ernst, R., et al. (2008). Assembly, configuration, and break-up history of Rodinia: A synthesis. *Precambrian Research*, *160*(1), 179–210. https://doi.org/10.1016/j.precamres.2007.04.021
Li, Z.-X., Li, X., Kinny, P., Wang, J., Zhang, S., & Zhou, H. (2003). Geochronology of Neoproterozoic syn-rift magmatism in the Yangtze Craton, South China and correlations with other continents: Evidence for a mantle superplume that broke up Rodinia. *Precambrian Research*, *122*(1), 85–109. https://doi.org/10.1016/S0301-9268(02)00208-5
Liou, J. G., Zhang, R. Y., Liu, F. L., Zhang, Z. M., & Ernst, W. G. (2012). Mineralogy, petrology, U-Pb geochronology, and geologic evolution of the Dabie-Sulu classic ultrahigh-pressure metamorphic terrane, East-Central China. *American Mineralogist*, *97*(10), 1533–1543. https://doi.org/10.2138/am.2012.4169
Liu, Y., Hu, Z., Zong, K., Gao, C., Gao, S., Xu, J., & Chen, H. (2010). Reappraisement and refinement of zircon U-Pb isotope and trace element analyses by LA-ICP-MS. *Chinese Science Bulletin*, *55*(15), 1535–1546. https://doi.org/10.1007/s11434-010-3052-4
Liu, Y. S., Hu, Z. C., Gao, S., Gunther, D., Xu, J., Gao, C. G., & Chen, H. H. (2008). In situ analysis of major and trace elements of anhydrous minerals by LA-ICP-MS without applying an internal standard. *Chemical Geology*, *257*(1-2), 34–43. https://doi.org/10.1016/j.chemgeo.2008.08.004
Ludwig, K. R. (2003). User's manual for Isoplot 3.00: A geochronological toolkit for Microsoft Excel.
Lux, D. R., DeYoreo, J. J., Guldotti, C. V., & Decker, E. R. (1986). Role of plutonism in low-pressure metamorphic belt formation. *Nature*, *323*(6091), 794–797. https://doi.org/10.1038/323794a0
Mahar, E. M., Baker, J. M., Powell, R., Holland, T. J. B., & Howell, N. (1997). The effect of Mn on mineral stability in metapelites. *Journal of Metamorphic Geology*, *15*(2), 223–238. https://doi.org/10.1111/j.1525-1314.1997.00011.x
Martin, L. A. J., Rubatto, D., Crépisson, C., Hermann, J., Putlitz, B., & Vitale-Brovarone, A. (2014). Garnet oxygen analysis by SHRIMP-SI: Matrix corrections and application to high-pressure metasomatic rocks from Alpine Corsica. *Chemical Geology*, *374–375*, 25–36. https://doi.org/10.1016/j.chemgeo.2014.02.010
Matthews, A. (1994). Oxygen isotope geothermometers for metamorphic rocks. *Journal of Metamorphic Geology*, *12*(3), 211–219. https://doi.org/10.1111/j.1525-1314.1994.tb00017.x
McKenzie, D. (1978). Some remarks on the development of sedimentary basins. *Earth and Planetary Science Letters*, *40*(1), 25–32. https://doi.org/10.1016/0012-821X(78)90071-7
Michard, A. (1989). Rare earth element systematics in hydrothermal fluids. *Geochimica et Cosmochimica Acta*, *53*(3), 745–750. https://doi.org/10.1016/0016-7037(89)90017-3
Miller, C. F., & Stoddard, E. F. (1981). The role of manganese in the paragenesis of magmatic garnet: An example from the Old Woman-Piute Range, California. *Journal of Geology*, *89*(2), 233–246. https://doi.org/10.1086/628582
Nijland, T. G., & Touret, J. L. R. (2001). Replacement of graphic pegmatite by graphic albite-actinolite-clinopyroxene intergrowths (Mjåvatn, southern Norway). *European Journal of Mineralogy*, *13*(1), 41–50. https://doi.org/10.1127/0935-1221/01/0013-0041

Oliver, N. H. S., Cleverley, J. S., Mark, G., Pollard, P. J., Fu, B., Marshall, L. J., et al. (2004). Modeling the role of sodic alteration in the genesis of iron oxide-copper-gold deposits, Eastern Mount Isa Block, Australia. *Economic Geology*, *99*(6), 1145–1176. https://doi.org/10.2113/gsecongeo.99.6.1145

Olsen, K. H. (1995). *Continental rifts: Evolution, structure, tectonics*. Amsterdam: Elsevier.

O'Neil, J. R., & Taylor, H. P. (1967). The oxygen isotope and cation exchange chemistry of feldspars. *American Mineralogist*, *52*(9-10), 1414–1437.

Page, F. Z., Essene, E. J., Mukasa, S. B., & Valley, J. W. (2014). A garnet–zircon oxygen isotope record of subduction and exhumation fluids from the Franciscan Complex, California. *Journal of Petrology*, *55*(1), 103–131. https://doi.org/10.1093/petrology/egt062

Page, F. Z., Kita, N. T., & Valley, J. W. (2010). Ion microprobe analysis of oxygen isotopes in garnets of complex chemistry. *Chemical Geology*, *270*(1), 9–19. https://doi.org/10.1016/j.chemgeo.2009.11.001

Platt, J., & England, P. (1994). Convective removal of lithosphere beneath mountain belts—Thermal and mechanical consequences. *American Journal of Science*, *294*(3). https://doi.org/10.2475/ajs.294.3.307

Powell, R., & Holland, T. (1999). Relating formulations of the thermodynamics of mineral solid solutions: Activity modeling of pyroxenes, amphiboles, and micas. *American Mineralogist*, *84*(1-2), 1–14. https://doi.org/10.2138/am-1999-1-201

Powell, R., & Holland, T. J. B. (1988). An internally consistent dataset with uncertainties and correlations: 3. Applications to geobarometry, worked examples and a computer program. *Journal of Metamorphic Geology*, *6*(2), 173–204. https://doi.org/10.1111/j.1525-1314.1988.tb00415.x

Putnis, A., & Putnis, C. V. (2007). The mechanism of reequilibration of solids in the presence of a fluid phase. *Journal of Solid State Chemistry*, *180*(5), 1783–1786. https://doi.org/10.1016/j.jssc.2007.03.023

Rubatto, D., & Angiboust, S. (2015). Oxygen isotope record of oceanic and high-pressure metasomatism: A P-T-time-fluid path for the Monviso eclogites (Italy). *Contributions to Mineralogy and Petrology*, *170*(5-6), 1–16. https://doi.org/10.1007/s00410-015-1198-4

Ruppel, C. (1995). Extensional processes in continental lithosphere. *Journal of Geophysical Research*, *100*(B12), 24,187–24,215. https://doi.org/10.1029/95JB02955

Russell, A. K., Kitajima, K., Strickland, A., Medaris, L. G., Schulze, D. J., & Valley, J. W. (2013). Eclogite-facies fluid infiltration: Constraints from $\delta^{18}O$ zoning in garnet. *Contributions to Mineralogy and Petrology*, *165*(1), 103–116. https://doi.org/10.1007/s00410-012-0794-9

Sandiford, M., & Powell, R. (1986). Deep crustal metamorphism during continental extension: Modern and ancient examples. *Earth and Planetary Science Letters*, *79*(1), 151–158. https://doi.org/10.1016/0012-821X(86)90048-8

Sengör, A. M. C., & Burke, K. (1978). Relative timing of rifting and volcanism on Earth and its tectonic implications. *Geophysical Research Letters*, *5*(6), 419–421. https://doi.org/10.1029/GL005i006p00419

Sharp, Z. D. (1995). Oxygen isotope geochemistry of the Al_2SiO_5 polymorphs. *American Journal of Science*, *295*(9), 1058–1076. https://doi.org/10.2475/ajs.295.9.1058

Smith, M. P., Henderson, P., Jeffries, T. E. R., Long, J., & Williams, C. T. (2004). The rare earth elements and uranium in garnets from the Beinn an Dubhaich aureole, Skye, Scotland, UK: Constraints on processes in a dynamic hydrothermal system. *Journal of Petrology*, *45*(3), 457–484. https://doi.org/10.1093/petrology/egg087

Solomon, G. C., & Taylor, H. P. (1991). Oxygen isotope studies of Jurassic fossil hydrothermal systems, Mojave Desert, southeastern California. *Geological Society, Special Publication*, *3*, 449–462.

Spear, F. S., & Kohn, M. J. (1996). Trace element zoning in garnet as a monitor of crustal melting. *Geology*, *24*(12), 1099–1102. https://doi.org/10.1130/0091-7613(1996)024<1099:TEZIGA>2.3.CO;2

Stacey, J. S., & Kramers, J. D. (1975). Approximation of terrestrial lead isotope evolution by a two-stage model. *Earth and Planetary Science Letters*, *26*(2), 207–221. https://doi.org/10.1016/0012-821X(75)90088-6

Sun, S.-S., & McDonough, W. F. (1989). Chemical and isotopic systematics of oceanic basalts: Implications for mantle composition and processes. *Geological Society of London, Special Publication*, *42*(1), 313–345. https://doi.org/10.1144/GSL.SP.1989.042.01.19

Symmes, G. H., & Ferry, J. M. (1992). The effect of whole-rock MnO content on the stability of garnet in pelitic schists during metamorphism. *Journal of Metamorphic Geology*, *10*(2), 221–237. https://doi.org/10.1111/j.1525-1314.1992.tb00080.x

Tang, J., Zheng, Y.-F., Gong, B., Wu, Y.-B., Gao, T.-S., Yuan, H., & Wu, F.-Y. (2008). Extreme oxygen isotope signature of meteoric water in magmatic zircon from metagranite in the Sulu orogen, China: Implications for Neoproterozoic rift magmatism. *Geochimica et Cosmochimica Acta*, *72*(13), 3139–3169. https://doi.org/10.1016/j.gca.2008.04.017

Taylor, H. P. (1977). Water/rock interactions and the origin of H_2O in granitic batholiths. *Journal of the Geological Society*, *133*(6), 509–558. https://doi.org/10.1144/gsjgs.133.6.0509

Taylor, H. P. (1990). Oxygen and hydrogen isotope constraints on the deep circulation of surface waters into zones of hydrothermal metamorphism and melting. In *The Role of Fluids in Crustal Processes* (pp. 72–95). Washington, DC: National Academy Press.

Trommsdorff, V., Piccardo, G., & Montrasio, A. (1993). From magmatism through metamorphism to sea floor emplacement of subcontinental Adria lithosphere during pre-Alpine rifting (Malenco, Italy). *Schweizerische Mineralogische und Petrographische*, *73*(2), 191–203.

Valley, J. W., Kinny, P. D., Schulze, D. J., & Spicuzza, M. J. (1998). Zircon megacrysts from kimberlite: Oxygen isotope variability among mantle melts. *Contributions to Mineralogy and Petrology*, *133*(1-2), 1–11. https://doi.org/10.1007/s004100050432

Valley, J. W., Kitchen, N., Kohn, M. J., Niendorf, C. R., & Spicuzza, M. J. (1995). UWG-2, a garnet standard for oxygen isotope ratios: Strategies for high precision and accuracy with laser heating. *Geochimica et Cosmochimica Acta*, *59*(24), 5223–5231. https://doi.org/10.1016/0016-7037(95)00386-X

Vielzeuf, D., Veschambre, M., & Brunet, F. (2005). Oxygen isotope heterogeneities and diffusion profile in composite metamorphic-magmatic garnets from the Pyrenees. *American Mineralogist*, *90*(2-3), 463–472. https://doi.org/10.2138/am.2005.1576

Wang, J., & Li, Z.-X. (2003). History of Neoproterozoic rift basins in South China: Implications for Rodinia break-up. *Precambrian Research*, *122*(1), 141–158. https://doi.org/10.1016/S0301-9268(02)00209-7

Wang, Z., Wang, J., Duan, T., Xie, Y., Zhuo, J., & Yang, P. (2010). Geochronology of middle Neoproterozoic volcanic deposits in Yangtze Craton interior of South China and its implications to tectonic settings. *Science China Earth Sciences*, *53*(9), 1307–1315. https://doi.org/10.1007/s11430-010-4012-1

White, R. S., Spence, G. D., Fowler, S. R., McKenzie, D. P., Westbrook, G. K., & Bowen, A. N. (1987). Magmatism at rifted continental margins. *Nature*, *330*, 439–444. https://doi.org/10.1038/330439a0

White, R. W., Pomroy, N. E., & Powell, R. (2005). An in situ metatexite–diatexite transition in upper amphibolite facies rocks from Broken Hill, Australia. *Journal of Metamorphic Geology*, *23*(7), 579–602. https://doi.org/10.1111/j.1525-1314.2005.00597.x

White, R. W., Powell, R., & Holland, T. J. B. (2007). Progress relating to calculation of partial melting equilibria for metapelites. *Journal of Metamorphic Geology*, *25*(5), 511–527. https://doi.org/10.1111/j.1525-1314.2007.00711.x

Wickham, S. M., & Oxburgh, E. R. (1985). Continental rifts as a setting for regional metamorphism. *Nature*, *318*(6044), 330–333. https://doi.org/10.1038/318330a0

Wickham, S. M., & Oxburgh, E. R. (1986). A rifted tectonic setting for Hercynian high-thermal gradient metamorphism in the Pyrenees. *Tectonophysics*, *129*(1-4), 53–69. https://doi.org/10.1016/0040-1951(86)90245-3

Wickham, S. M., & Taylor, H. P. (1987). Stable isotope constraints on the origin and depth of penetration of hydrothermal fluids associated with Hercynian regional metamorphism and crustal anatexis in the Pyrenees. *Contributions to Mineralogy and Petrology*, *95*(3), 255–268. https://doi.org/10.1007/BF00371841

Wilson, J. T. (1966). Did the Atlantic close and then re-open? *Nature*, *211*, 676–681. https://doi.org/10.1038/211676a0

Wu, Y.-B., Zheng, Y.-F., Tang, J., Gong, B., Zhao, Z.-F., & Liu, X. (2007). Zircon U–Pb dating of water–rock interaction during Neoproterozoic rift magmatism in South China. *Chemical Geology*, *246*(1-2), 65–86. https://doi.org/10.1016/j.chemgeo.2007.09.004

Yang, Z., Sun, Z., Yang, T., & Pei, J. (2004). A long connection (750–380 Ma) between South China and Australia: Paleomagnetic constraints. *Earth and Planetary Science Letters*, *220*(3), 423–434. https://doi.org/10.1016/S0012-821X(04)00053-6

Zakharov, D. O., Bindeman, I. N., Slabunov, A. I., Ovtcharova, M., Coble, M. A., Serebryakov, N. S., & Schaltegger, U. (2017). Dating the Paleoproterozoic snowball Earth glaciations using contemporaneous subglacial hydrothermal systems. *Geology*, *45*(7), 667–670. https://doi.org/10.1130/G38759.1

Zhang, S.-B., & Zheng, Y.-F. (2013). Formation and evolution of Precambrian continental lithosphere in South China. *Gondwana Research*, *23*(4), 1241–1260. https://doi.org/10.1016/j.gr.2012.09.005

Zheng, Y.-F. (1993). Calculation of oxygen isotope fractionation in anhydrous silicate minerals. *Geochimica et Cosmochimica Acta*, *57*, 1079–1079. https://doi.org/10.1016/0016-7037(93)90042-U

Zheng, Y.-F., & Chen, R.-X. (2017). Regional metamorphism at extreme conditions: Implications for orogeny at convergent plate margins. *Journal of Asian Earth Sciences*, *145*, 46–73. https://doi.org/10.1016/j.jseaes.2017.03.009

Zheng, Y.-F., Chen, R.-X., & Zhao, Z.-F. (2009). Chemical geodynamics of continental subduction-zone metamorphism: Insights from studies of the Chinese Continental Scientific Drilling (CCSD) core samples. *Tectonophysics*, *475*(2), 327–358. https://doi.org/10.1016/j.tecto.2008.09.014

Zheng, Y.-F., & Fu, B. (1998). Estimation of oxygen diffusivity from anion porosity in minerals. *Geochemical Journal*, *32*(2), 71–89. https://doi.org/10.2343/geochemj.32.71

Zheng, Y.-F., Fu, B., Gong, B., & Li, L. (2003). Stable isotope geochemistry of ultrahigh pressure metamorphic rocks from the Dabie–Sulu orogen in China: Implications for geodynamics and fluid regime. *Earth-Science Reviews*, *62*(1-2), 105–161. https://doi.org/10.1016/S0012-8252(02)00133-2

Zheng, Y. F., Gong, B., Zhao, Z. F., Wu, Y. B., & Chen, F. K. (2008). Zircon U-Pb age and O isotope evidence for Neoproterozoic low-^{18}O magmatism during supercontinental rifting in South China: Implications for the snowball Earth event. *American Journal of Science*, *308*(4), 484–516. https://doi.org/10.2475/04.2008.04

Zheng, Y.-F., Wu, Y.-B., Chen, F.-K., Gong, B., Li, L., & Zhao, Z.-F. (2004). Zircon U-Pb and oxygen isotope evidence for a large-scale ^{18}O depletion event in igneous rocks during the Neoproterozoic. *Geochimica et Cosmochimica Acta*, *68*(20), 4145–4165. https://doi.org/10.1016/j.gca.2004.01.007

Zheng, Y.-F., Wu, Y.-B., Gong, B., Chen, R.-X., Tang, J., & Zhao, Z.-F. (2007). Tectonic driving of Neoproterozoic glaciations: Evidence from extreme oxygen isotope signature of meteoric water in granite. *Earth and Planetary Science Letters*, *256*(1–2), 196–210. https://doi.org/10.1016/j.epsl.2007.01.026

Zheng, Y.-F., Xiao, W.-J., & Zhao, G. (2013). Introduction to tectonics of China. *Gondwana Research*, *23*(4), 1189–1206. https://doi.org/10.1016/j.gr.2012.10.001

Zheng, Y.-F., & Zhao, Z.-F. (2017). Introduction to the structures and processes of subduction zones. *Journal of Asian Earth Sciences*, *145*, 1–15. https://doi.org/10.1016/j.jseaes.2017.06.034

Zheng, Y.-F., Zhao, Z.-F., & Chen, R.-X. (2019). Ultrahigh-pressure metamorphic rocks in the Dabie–Sulu orogenic belt: Compositional inheritance and metamorphic modification. *Geological Society of London, Special Publication*, *474*, 89–132. https://doi.org/10.1144/SP474.9

Zheng, Y.-F., Zhao, Z.-F., Wu, Y.-B., Zhang, S.-B., Liu, X., & Wu, F.-Y. (2006). Zircon U–Pb age, Hf and O isotope constraints on protolith origin of ultrahigh-pressure eclogite and gneiss in the Dabie orogen. *Chemical Geology*, *231*(1), 135–158. https://doi.org/10.1016/j.chemgeo.2006.01.005

Zheng, Y.-F., Zhou, J.-B., Wu, Y.-B., & Xie, Z. (2005). Low-grade metamorphic rocks in the Dabie-Sulu orogenic belt: A passive-margin accretionary wedge deformed during continent subduction. *International Geology Review*, *47*(8), 851–871. https://doi.org/10.2747/0020-6814.47.8.851

Ziegler, P. A., & Cloetingh, S. (2004). Dynamic processes controlling evolution of rifted basins. *Earth-Science Reviews*, *64*(1-2), 1–50. https://doi.org/10.1016/S0012-8252(03)00041-2